國立交通大學

電子工程學系　電子研究所

碩 士 論 文

新穎六層 $k \cdot p$ 模擬器用於受應力(001)及(110)P型複晶矽，全矽化

及金屬閘極P通道金氧半場效電晶體之閘極電洞穿隧電流

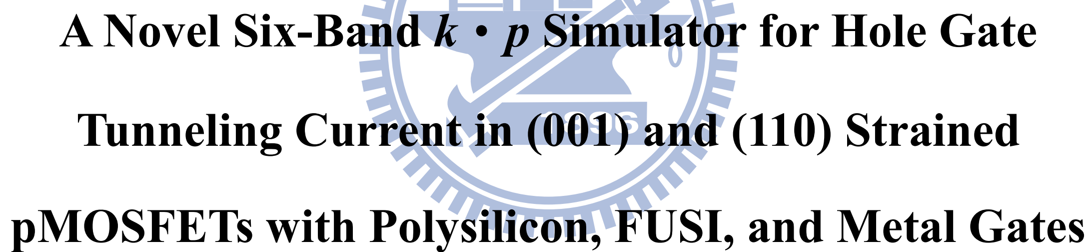

A Novel Six-Band $k \cdot p$ Simulator for Hole Gate

Tunneling Current in (001) and (110) Strained

pMOSFETs with Polysilicon, FUSI, and Metal Gates

研 究 生: 彭霖祥　　Lim-Shyang Pee

指導教授: 陳明哲 博士　Prof. Ming-Jer Chen

中華民國 一００年 八 月

新穎六層 $k \cdot p$ 模擬器用於受應力(001)及(110)Ｐ型複晶矽，全矽化及金屬閘極Ｐ通道金氧半場效電晶體之閘極電洞穿隧電流

A Novel Six-Band $k \cdot p$ Simulator for Hole Gate Tunneling Current in (001) and (110) Strained pMOSFETs with Polysilicon, FUSI, and Metal Gates

研究生：彭霖祥　　Lim-Shyang Pee

指導教授：陳明哲　　Prof. Ming-Jer Chen

國立交通大學

電子工程學系　電子研究所

碩士論文

A Thesis

Submitted to Department of Electronics Engineering & Institute of Electronics

College of Electrical and Computer Engineering

National Chiao Tung University

in Partial Fulfillment of the Requirements

for the Degree of

Master of Science

in

Electronics Engineering

August 2011

Hsinchu, Taiwan, Republic of China

中華民國 一００ 年 八 月

新穎六層 $k \cdot p$ 模擬器用於受應力(001)及(110) P型複晶矽，全矽化及金屬閘極P通道金氧半場效電晶體之閘極電洞穿隧電流

研究生: 彭霖祥　　　　　　指導教授: 陳明哲 博士

國立交通大學

電子工程學系 電子研究所碩士班

摘要

本論文所提出嶄新進階式有效質量近似的演算法可以直接且有效的計算受應力下(001)及(110)晶向P通道金氧半場效電晶體的閘極電洞穿隧電流·文中也提及傳統的六層 kp 模型及舊式與進階式的有效質量近似的比較·此演算法已透過幾道程序性的驗證，如(一)自身若合符節的電容與閘極電壓曲線重建;(二)在受應力下的P型複晶矽，全矽化(ＦＵＳＩ)及金屬閘極P通道金氧半電晶體晶都有令人滿意的實驗值與模擬值的比較;(三)應力值達負３ＧＰａ對遷移率的增益與已發表的文獻相當一致;以及(四)在有應力及沒有應力的鰭式場效電晶體(ＦｉｎＦＥＴ)(１１０)側壁所發表的文獻實驗值也一一被重建出來·除此之外，透過此進階式有效質量近似的演算法，我們可以觀察與分析在P型複晶矽閘極P通道金氧半電晶體(負１·８３ GPA)與全矽化閘極P通道金氧半電晶體(負２·２９ GPA)所造成閘極電洞穿隧電流不同的起因·

A Novel Six-Band $k \cdot p$ Simulator for Hole Gate Tunneling Current in (001) and (110) Strained pMOSFETs with Polysilicon, FUSI, and Metal Gates

Student: Lim-Shyang Pee Advisor: Dr. Ming-Jer Chen

Department of Electronics Engineering and Institute of Electronics

National Chiao Tung University

Abstract

We present an enhanced effective mass approximation (eEMA) algorithm with which one can straightforwardly calculate hole gate tunneling current Ig in (001) and (110) uniaxial compressive strained p-MOSFETs. The differences among the conventional EMA, enhanced EMA, and sophisticated six-band k dot p results are demonstrated. The algorithm is systematically validated in the various ways: (i) self-consistent Cg-Vg curve reproduction; (ii) satisfactory fitting of existing strain altered Ig data for both polysilicon, fully-silicided (FUSI), and metal gates; (iii) good agreement with literature mobility enhancement values for stress up to -3 GPa; and (iv) reasonable fitting of available experimental Ig-Vg curves in (110) sidewall-surface p-FinFETs with and without the stress. Moreover, with the use of the algorithm we can examine the origins of the observed Ig difference between polysilicon gate p-MOSFETs (-1.83 GPa) and FUSI ones (-2.29 GPa).

Acknowledgements

My wonderful time at 309A passed quickly, but it left me a lot of sweet and unforgettable memories. It is my great honor to meet Prof. Chen, and to have him to be my advisor. Thanks to Prof. Chen for the guidance and tutor on my master study and even the morals of being human. I will always remember the useful "slogan" that you always remind us on research: back to the origin. Thanks to my dearest family for encouraging me all the time either mentally or financially. Thanks to my "boss", C.C. Lee for providing instruction and assistance on my research, it is my pleasure to work and cooperate with you.

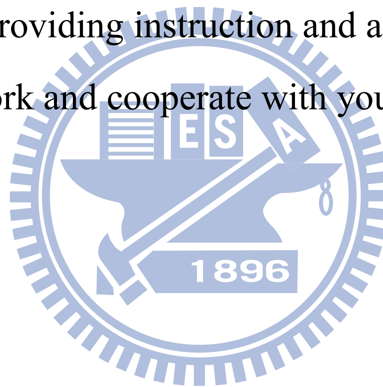

Contents

Chinese Abstract I

English Abstract II

Acknowledgements III

Contents IV

Figure Captions VI

Table Captions XI

Chapter 1 Introduction 1

Chapter 2 Enhanced EMA Algorithm 3

2.1 Introduction 3

2.2 Strain and Surface Orientation 3

2.2.1 k・p Hamiltonian 3

2.2.2 Stress Effect 4

2.2.3 Surface Orientation Effect 5

2.3 Enhanced EMA (eEMA) Algorithm 6

2.4 Validation of eEMA 8

Chapter 3 eEMA Orientated Simulation Results 10

Introduction 10

3.1 Capacitance versus Gate Voltage 10

3.2 Hole Gate Direct Tunneling Current 11

3.2.1 Physical Model 11

3.2.2 Simulation Result and Discussion 13

Chapter 4 Individual Contributions to 40% Gate Current Reduction in FUSI Gate Strained (001) p-MOSFETs 15

4.1 Introduction 15

4.2 Parameter Extraction......15

4.3 Simulation Result and Discussion 16

Chapter 5 Conclusion 18

References 19

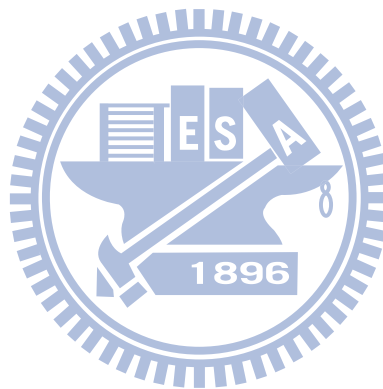

Figure Captions

Fig. 2.1The flowchart of our enhanced EMA algorithm. In the inserted equations, $E1,v$ is the first subband of the vth bulk band $Ev0$, and $DOS1,vE$ is the density-of-states function for $E1,v$. Fs is the surface field, q is the free electron charge, and $f(E)$ is the Fermi-Dirac distribution. 24

Fig. 2.2 The device structures for (001) and (110) p-MOSFETs. The channel direction and applied stress direction are clarified. Here, only the favorable longitudinal compressive stress is under study. 25

Fig. 2.4.1 The resulting (001) effective masses for H1 bulk band versus surface bending. The heavy, light, and split-off holes, for each subband energy, are mixed due to the coupling effect from the surface quantum confinement or the strain effect [7]. Therefore, we group the subband energies mainly according to the three lowest bulk bands, $E10$(H1), $E20$(H2), and $E30$(H3). 27

Fig. 2.4.2 The resulting (001) effective masses for H2 bulk band. The orange dashed lines refer to the constant effective masses as in unstressed conditions. 28

Fig. 2.4.3 The resulting (001) effective masses for H3 bulk band. 29

Fig. 2.4.4 The resulting (110) effective masses for H1 bulk band. Only H1 and H2 bulk bands are shown in (110) case here because of their high occupation in the subband energies. Note that (110) $mQNH1$ is stress sensitive. 30

Fig. 2.4.5 The resulting (110) effective masses for H2 bulk band. 31

Fig. 2.4.6 The comparison of subband energy of (001) without stress among fully-iterated, eEMA and constant EMA. 32

Fig. 2.4.7 The comparison of subband energy of (001) under longitudinal compressive stress 1 GPa among fully-iterated, eEMA and constant

EMA...33
Fig 2.4.8 The comparison of subband energy of (001) under longitudinal compressive stress 3 GPa among fully-iterated, eEMA and constant EMA...34

Fig. 2.4.9 The comparison of subband energy of (110) without stress among fully-iterated, eEMA and constant EMA. 35

Fig. 2.4.10 The comparison of subband energy of (110) under longitudinal compressive stress 1 GPa among fully-iterated, eEMA and constant EMA...36

Fig. 2.4.11 The comparison of subband energy of (110) under longitudinal compressive stress 3 GPa among fully-iterated, eEMA and constant EMA...37

Fig. 3.1.1 The comparison of calculated non-stress (001) gate capacitance versus gate voltage from the constant EMA and enhanced EMA with the sophisticated six-band k·p results. 38

Fig. 3.1.2 The comparison of calculated non-stress (110) gate capacitance versus gate voltage from the constant EMA and enhanced EMA with the sophisticated six-band k·p results. 39

Fig. 3.2.2.1 The calculated hole gate direct tunneling current density for (001) and (110) p-MOSFETs under the longitudinal stress conditions of 0, -1, and -3 GPa. It is contributed by four parts: 1) $F_{i,v}$ impact frequency of hole wave packet on interface, 2) $n_{i,v}(E)$inversion carrier density per energy, 3) $T_{i,v}^{WKB}$ WKB part of transmission probability through insulator, and 4) $T_{i,v}^{R}$ reflection part of transmission probability through insulator...40

Fig. 3.2.2.2 The contribution of the averaged impact frequency of hole wave packet on interface for (001) and (110) p-MOSFETs under the longitudinal stress conditions of 0, -1, and -3 GPa. 41

Fig. 3.2.2.3 The contributions of the total inversion carrier density for (001) and (110) p-MOSFETs under the longitudinal stress conditions of 0, -1, and -3 GPa. 42

Fig. 3.2.2.4 The contributions of the average WKB transmission probability through insulator for (001) and (110) p-MOSFETs under the longitudinal stress conditions of 0, -1, and -3 GPa. 43

Fig. 3.2.2.5 The contribution of the average reflection part of transmission probability through insulator for (001) and (110) p-MOSFETs under the longitudinal stress conditions of 0, -1, and -3 GPa. 44

Fig. 3.2.2.6 Schematic of energy band diagram of (110) p-MOSFET to show the effective mass correction in p+-poly gate region. The two group velocities are associated with the effective masses labeled. 45

Fig. 3.2.2.7 The comparison of experimental and calculated hole gate direct tunneling current change versus stress. The bias conditions and process parameters in the calculation are close to the experimental ones, where $|V_G|$~1V for polygate and $|V_G|$~1.6V for metal gate. 46

Fig. 3.2.2.8 The calculated hole gate direct tunneling current change as in Fig. 3.3.2.7 but with the stress range largely widened. The inset shows simulated mobility enhancement and its comparison with [19]. 47

Fig. 3.2.2.9 The comparison of calculated hole gate direct tunneling current for p-FinFET with those measured from (110) sidewall surface p-FinFET [2]. 48

Fig. 3.2.2.10 The calculated hole gate direct tunneling current density for (001) p-MOSFETs with polysilicon, FUSI and metal gates under the longitudinal stress conditions of 0 and -2.5 GPa. 49

Fig. 3.2.2.11 The calculated hole gate direct tunneling current density for (110) p-MOSFETs with polysilicon, FUSI and metal gates under the longitudinal stress conditions of 0 and -2.5 GPa. 50

1896

Fig. 3.2.2.12 The calculated hole gate direct tunneling current change versus stress for (001) and (110) p-MOSFETs with polysilicon, FUSI and metal gates. 51

Fig. 4.2.1 Capacitance-voltage fitting through proposed eEMA on (100) p-MOSFETs with polysilicon and FUSI gates. The experimental data is measured under large devices. FUSI imposes an extra compressive stress ~460 MPa on the underlying p-MOSFET channel region. Table I shows the extracted parameters. 52

Fig. 4.2.2 Jg versus gate overdrive fitting under the small dimension samples. Solid symbols indicate the experimental data and open symbols with line indicate the calculated one. The gate overdrive is used to eliminate Vth roll-off appearing in FUSI gate as shown in insert, so both the inversion conditions are same: Vth(Lmask=1um) for the ideal calculation results and Vth(Lmask=0.036um) for the experimental results. 53

Fig. 4.3.1 Comparison of CV fitting on (100) p-MOSFETs with polysilicon and FUSI gates. (a) without consideration of stress on FUSI gate. (b) Longitudinal compressive stress 460 MPa considered on FUSI gate, which fitted perfectly. 54

Fig. 4.3.2 Impact of polysilicon dopant concentration on (a) capacitance-voltage curve and (b) Ig versus Vg . $Nsub = 1 \times 1018cm - 3, Tox = 1.3nm , moxh = 0.37m0$, Stress = Long. −1.83 GPa..55

Fig. 4.3.3 Impact of Longitudinal compressive stress on (a) capacitance-voltage curve and (b) Ig versus Vg . $Nsub = 1 \times 1018cm - 3, Tox = 1.3nm , moxh = 0.37m0 , Npoly = 7 \times 1019cm - 3$..56

Fig. 4.3.4 Impact of work function shift on (a) Capacitance-voltage curve and (b) Ig versus Vg . $Nsub = 1 \times 1018cm - 3, Tox = 1.3nm , moxh = 0.37m0$, without stress..57

Fig. 4.3.5 The calculated hole gate direct tunneling currents for polysilicon- and FUSI-gate p-MOSFETs and the comparison with two data points [24]. The inset depicts the five main contributions for the observed hole gate direct tunneling current difference. 58

Fig. 4.3.6 The comparison of work function of Ni FUSI gates among this work, [26] and [27]. The additional dopants to polysilicon before silicidation result the shifts in work function.....................................59

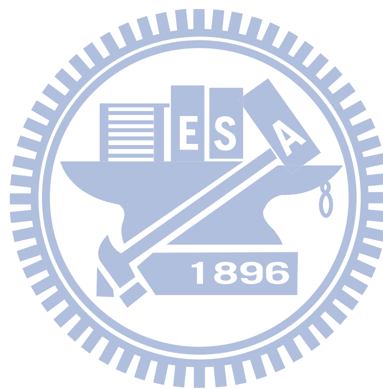

Table Captions

Table I. The extracted parameters for Fig 4.2.1 and 4.2.2.

Table II. Hole band, hole scattering and physical parameters used in this work

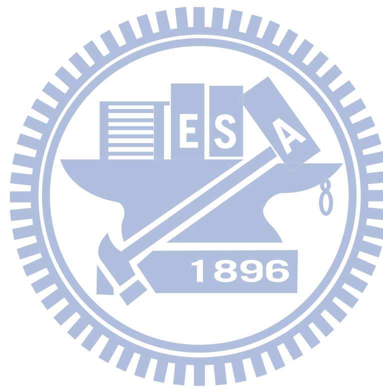

Chapter 1
Introduction

Owing to the successful effective mass approximation (EMA) in inversion layers of n-MOSFETs, it is possible to develop a gate direct tunneling model [1]. However, in the presence of the anisotropic and non-parabolic properties around Γ point of the valence-band structure, the ability to quantitatively deal with the hole effective masses in p-MOSFETs has long been one of the challenging issues. Currently, both the strain engineering and the p-FinFET structure with (110) sidewall surface have raised this concern further [2]. Sophisticated simulations [3],[4] have already quantified hole effective masses, primarily on (001) surface only. Although there exist some works [5],[6] dedicated to the strain and (110) orientation effects on effective masses, extensions to the hole gate direct tunneling current Ig were not yet done. Even in the citation [2], a conversion from measured stress altered threshold voltage to effective mass change was needed prior to Ig calculation. Here, we propose an enhanced EMA algorithm, based on our recent work [4], to achieve the goal directly, without accounting for the conversion procedure [2].

Firstly, the flowchart of enhanced EMA will be explained in Chapter 2. The process of extracting the quantization and two-dimensional DOS effective masses will be demonstrated. In addition, the simulated effective masses will be shown with the accompanying subband energies. Next, the capacitance and gate direct tunneling current calculation under the varying stress and wafer orientations will be exhibited in Chapter 3. The supporting experimental results will be also shown and discussed. Then, Chapter 4 is devoted to examine the twofold difference in hole gate direct tunneling current between FUSI and polysilicon gate. Finally, the conclusions will be given in

Chapter 5.

Chapter 2
Enhanced EMA Algorithm

2.1 Introduction

It has been well recognized that in the context of the effective mass approximation (EMA), a two-dimensional electron gas (2DEG) system in n-channel MOSFETs can be visualized and described successfully in a quasi-classical manner. However, the valence-band structure of inversion layers in p-MOSFETs is much complicated in terms of strong anisotropy and nonparabolicity of the hole subbands. As discussed in our previous work [4], the effective masses enable the acceleration of fully iterated six-band k dot p Schrödinger and Poisson numerical loop. Here, we propose an enhanced EMA algorithm in order to calculate hole gate direct tunneling current Ig in (001) and (110) under strain effects. Fig. 2.1 shows the flowchart of our enhanced EMA algorithm. Fig. 2.2 clarifies the effects of the in-plane stress and channel direction in (001) and (110) p-MOSFETs. We will first discuss how the strain and surface orientation effect can be treated in our $k \cdot p$ Hamiltonian H_{kp}. Then, we extract both the quantization effective mass m_{QN} and DOS effective mass m_{DOS}, followed by the validation of this proposed eEMA.

2.2 Strain and Surface Orientation

2.2.1 k・p Hamiltonian

The $k \cdot p$ Hamiltonian H_{kp} used in our algorithm is composed of two parts: the Luttinger-Kohn Hamiltonian H_{LK} and the strain Hamiltonian H_{strain}. These expressions can be described in terms of the following 6×6 Hamiltonian [7]:

$$H_{kp} = H_{LK} + H_{strain} = \begin{bmatrix} -P-Q & L & -M & 0 & \frac{1}{\sqrt{2}}L & -\sqrt{2}M \\ L^{+} & -P+Q & 0 & -M & \sqrt{2}Q & -\sqrt{\frac{3}{2}}L \\ -M^{+} & 0 & -P+Q & -L & -\sqrt{\frac{3}{2}}L^{+} & -\sqrt{2}Q \\ 0 & -M^{+} & -L^{+} & -P-Q & \sqrt{2}M^{+} & \frac{1}{\sqrt{2}}L^{+} \\ \frac{1}{\sqrt{2}}L^{+} & \sqrt{2}Q^{+} & -\sqrt{\frac{3}{2}}L & \sqrt{2}M & -P-\Delta & 0 \\ -\sqrt{2}M^{+} & -\sqrt{\frac{3}{2}}L^{+} & -\sqrt{2}Q^{+} & \frac{1}{\sqrt{2}}L & 0 & -P-\Delta \end{bmatrix}, \quad (2.2.1.1)$$

where

$$\begin{aligned} P &= P_k + P_\varepsilon \\ Q &= Q_k + Q_\varepsilon \\ L &= L_k + L_\varepsilon \\ M &= M_k + M_\varepsilon \end{aligned}, \quad (2.2.1.2)$$

$$\begin{aligned} P_k &= \frac{\hbar}{2m_0}\gamma_1\left(\kappa_x + k_y^2 + k_z^2\right) \\ Q_k &= \frac{\hbar}{2m_0}\gamma_2\left(\kappa_x + k_y^2 - 2k_z^2\right) \\ L_k &= \frac{\hbar}{m_0}\sqrt{3}\gamma_3\left(\kappa_x - ik_y\right)k_z \\ M_k &= -\frac{\hbar}{2m_0}\sqrt{3}\left[\gamma_2\left(k_x^2 - k_y^2\right) - 2i\gamma_3 k_x k_y\right] \end{aligned} ; \quad \begin{aligned} P_\varepsilon &= -a_v\left(\varepsilon_{xx} + \varepsilon_{yy} + \varepsilon_{zz}\right) \\ Q_\varepsilon &= -\frac{b}{2}\left(\varepsilon_{xx} + \varepsilon_{yy} - 2\varepsilon_{zz}\right) \\ L_\varepsilon &= -d\left(\varepsilon_{xz} - i\varepsilon_{yz}\right) \\ M_\varepsilon &= \frac{\sqrt{3}}{2}b\left(\varepsilon_{xx} - \varepsilon_{yy}\right) - id\varepsilon_{xy} \end{aligned} . \quad (2.2.1.3)$$

The P_k, Q_k, L_k and M_k are the $k \cdot p$ terms and the P_ε, Q_ε, L_ε and M_ε are the strain terms, which will be discussed later. The Δ is the split-off energy. The Luttinger parameters γ_1, γ_2, γ_3 and strain deformation potentials a_v, b, d are both listed in Table II.

2.2.2 Stress Effect

Strain describes the change of size and/or shape in response to external forces which are applied on a deformable body; however, stress is defined as the average amount of

force exerted per unit area. Gratefully, a general form originating from Hooke's law was developed, which can adequately deal with the mechanics of materials, as expressed below [8]

$$\varepsilon_{xx} = \frac{1}{E}\left[\sigma_{xx} - \nu\left(\sigma_{yy} + \sigma_{zz}\right)\right] \quad (2.2.2.1a)$$

$$\varepsilon_{yy} = \frac{1}{E}\left[\sigma_{yy} - \nu(\sigma_{xx} + \sigma_{zz})\right] \quad (2.2.2.1b)$$

$$\varepsilon_{zz} = \frac{1}{E}\left[\sigma_{zz} - \nu\left(\sigma_{xx} + \sigma_{yy}\right)\right] \quad (2.2.2.1c)$$

$$\gamma_{xy} = \frac{1}{G}\tau_{xy}\ ,\ \gamma_{xz} = \frac{1}{G}\tau_{xz}\ ,\ \gamma_{yz} = \frac{1}{G}\tau_{yz} \quad (2.2.2.1\mathrm{d})$$

where σ_{ii} refers to the normal stress component acting on the planes perpendicular to i-direction, τ_{ij} indicates the shear stress components oriented in the j-direction acting on the planes perpendicular to i-direction, γ_{ij} denotes engineered shear strain, and ε_{ij} is average shear strain defined as one half the γ_{ij} [9], [10]. E, ν and G represent the Young's modules, Poisson's ratio and shear modulus of elasticity, respectively. We therefore establish the elastic strain-stress matrix in the following [11]:

$$\begin{bmatrix} \varepsilon_{xx} \\ \varepsilon_{yy} \\ \varepsilon_{zz} \\ 2\varepsilon_{yz} \\ 2\varepsilon_{zx} \\ 2\varepsilon_{xy} \end{bmatrix} = \begin{bmatrix} S_{11} & S_{12} & S_{12} & 0 & 0 & 0 \\ S_{12} & S_{11} & S_{12} & 0 & 0 & 0 \\ S_{12} & S_{12} & S_{11} & 0 & 0 & 0 \\ 0 & 0 & 0 & S_{44} & 0 & 0 \\ 0 & 0 & 0 & 0 & S_{44} & 0 \\ 0 & 0 & 0 & 0 & 0 & S_{44} \end{bmatrix} \begin{bmatrix} \sigma_{xx} \\ \sigma_{yy} \\ \sigma_{zz} \\ \tau_{yz} \\ \tau_{zx} \\ \tau_{xy} \end{bmatrix} \quad (2.2.2.2)$$

where S_{11}, S_{12} and S_{44} are the elastic stiffness constants. Those parameters used in our simulation are listed in Table II.

2.2.3 Surface Orientation Effect

Since the $k \cdot p$ Hamiltonian H_{kp} is established under the (001) systems, we need to do some appropriate rotations on k space for the purpose of dealing with (110), (111), (112) or even (11x) surface. For (110) surface, a rotation from the original (001) k space to (110) k' is required:

$$k'_x = -k_z$$

$$k'_y = \frac{1}{\sqrt{2}}(k_x - k_y) \qquad (2.2.3.1)$$

$$k'_z = \frac{1}{\sqrt{2}}(k_x + k_y)$$

for (111) surface:

$$k'_x = \frac{1}{\sqrt{6}}(k_x + k_y - k_z)$$

$$k'_y = \frac{1}{\sqrt{2}}(-k_x + k_y) \qquad (2.2.3.2)$$

$$k'_z = \frac{1}{\sqrt{3}}(k_x + k_y + k_z)$$

and likely for (112) surface:

$$k'_x = \frac{1}{\sqrt{3}}(k_x + k_y - k_z)$$

$$k'_y = \frac{1}{\sqrt{2}}(-k_x + k_y) \qquad (2.2.3.3)$$

$$k'_z = \frac{1}{\sqrt{6}}(k_x + k_y + 2k_z)$$

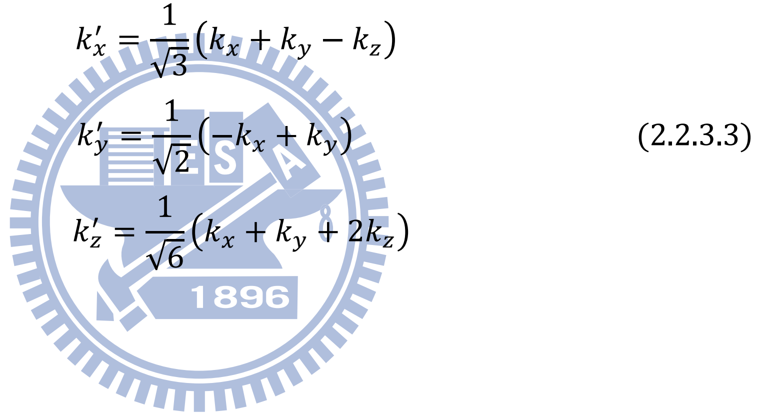

2.3 Enhanced EMA (eEMA) Algorithm

The self-consistent six-band k dot p simulation in inversion layers of p-MOSFETs is time-consuming. To simplify the hole subband structure calculation, a triangular-potential approximation may be employed [12]. In this algorithm, we first input an initial surface field to six-band k dot p schrodinger equation solver with triangular potential approximation. Each of the k states is systematically calculated on the decided k_x-k_y space accordingly. The outcomes of the triangular-potential-based six-band k dot p simulator contain the constant-energy contours in the k plane, the subband energy levels, the surface potential, and the Fermi level E_f of the sysyem. The

$\mathrm{E}(k)$ resulting from our six-band $k \cdot p$ calculation can be used to derive the density-of –states function for holes in the valence-band for semiconductor of interest. The corresponding two-dimensional density-of-states (***DOS***) functions are determined in the Cartesian coordinate system by

$$DOS_{1,v}(E) = U\left(E - E_{1,v}\right)\frac{1}{(2\pi)^2} \times \frac{Area_{1,v}^{k-space}(E+dE) - Area_{1,v}^{k-space}(E)}{dE} \quad (2.3.1)$$

where the index v means the subband order up to the sixth lowest subband and $U(E)$ means the unit step function of energy. The total ***DOS*** function is given as

$$DOS_{total}(E) = \sum_{v} DOS_{1,v}(E) \quad (2.3.2)$$

According to the calculations above, ***DOS*** effective mass of each subband is energy dependent, and each of them can be inversely extracted from simulated $DOS_{1,v}(E)$:

$$m_{DOS}^{1,v}(E) = 2\pi\hbar^2 \times DOS_{1,v}(E) \quad (2.3.3)$$

To obtain the ***DOS*** effective mass efficiently and accurately, we average them by

$$\langle m_{DOS}^{v} \rangle = \frac{\int m_{DOS}^{1,v}(E) f(E) \cdot DOS_{1,v}(E) dE}{\int f(E) \cdot DOS_{1,v}(E) dE} \quad (2.3.4)$$

Additionally, based on triangular potential approximation [13], the quantization effective mass, m_{QN}^{v}, can also be analytically derived as

$$m_{QN}^{v} = \frac{\hbar^2}{2}\left(E_{1,v} - E_{v}^{0}\right)^{-3}\left(\frac{3}{2}\pi q F_s \left(1 + \frac{3}{4}\right)\right)^2 \quad (2.3.5)$$

where $E_{1,v}$ is the first subband of the vth bulk band E_v^0, and $DOS_{1,v}(E)$ is the density-of-states function for $E_{1,v}$. F_s is the surface field, q is the free electron charge, and $f(E)$ is the Fermi-Dirac distribution. All the items above are from the results of the six-band k·p Schrödinger equation with the triangular potential approach. Worthy to note that the hole type distinguishing (e.g. heavy hole, light hole, and split-off hole, for each subband energy) is obscure due to the coupling between each other under the surface quantum confinement and/or the strain effect. The correlative study can be found in [14], which states that one subband may mix with three hole types. Therefore,

we group the subband energies *mainly* according to the three lowest bulk bands, E_1^0, E_2^0, and E_3^0 (we can say that $v = 1$ for heavy hole, $v = 2$ for light hole, and $v = 3$ for split-off hole with *no applied stress*). To recognize them easily, we call the $v = 1$ bulk band as *H1*, the $v = 2$ bulk band as *H2*, and the $v = 3$ bulk band as *H3*. For (001) case within the 0 to -3 GPa channel stress, we assume that the three lowest subband energies from triangular potential approach are $E_{1,H1}$, $E_{1,H2}$, and $E_{1,H3}$. But for (110) case, the three lowest subband energies from triangular potential approach are $E_{1,H1}$, $E_{2,H1}$, and $E_{1,H2}$.

Until now, both effective masses are readily to be served in the last but the most important section. Analogous to the electron counterparts [15], [16], the simple EMA-oriented Schrödinger-Poisson iterative solving can be employed using the aforementioned effective masses in the condition of the output surface field must nearly equal to the initial surface field. The EMA-oriented Schrödinger-Poisson iterative solving in pMOSFETs is therefore as fast as the nMOSFET, and finally the outputs are readily to be used, since its validity is seriously examined that will be given in next section

2.4 Validation of eEMA

Fig. 2.4.1 to 2.4.5 show the effective masses of each bulk band on (001) and (110) surfaces as the valleys in electron counterpart. The H1 and H2 quantization masses on (001) can be approximated or treated reasonably well by constant mass just like what had been published elsewhere [17], [18]. However, the quantization mass of (110) should not be described by constant mass, since we can see that (110) H1 quantization effective mass increases rapidly because of the compressive channel stress. This is directly related to the stressed bulk heavy-hole constant energy surface as shown in

the insert of Fig. 2.4.4. Only H1 and H2 bands are shown in (110) case because they are the most dominant bands. To use both effective mass conveniently, surface band bending is labeled on x-scale, so they can directly be applied in Schrödinger and Poisson self-consistent calculation. Extremely huge CPU time is inevitable if one has to run the six-band $k \cdot p$ calculation instead of using our simulation results. The corresponding subband energies and the subband comparison between the constant EMA, our enhanced EMA, and sophisticated six-band k·p results are also illustrated in Fig. 2.4.6 and 2.6.11. Thus, the validity of the enhanced EMA is confirmed by this comparison and it leads us to reach a clear conclusion: (i) the enhanced EMA remains its validity under various channel stresses on both (001) and (110) wafer orientations; and (ii) the result of enhanced EMA can find further application in gate capacitance and gate direct tunneling current.

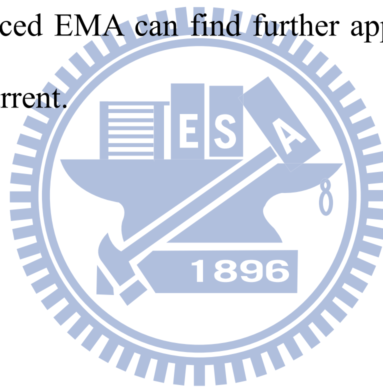

Chapter 3
eEMA Orientated Simulation Results

Introduction

In this section, we check the reliability of our simulated capacitance and the hole gate direct tunneling current in (001) and (110) uniaxial compressive strained p-MOSFETs with the effective mass obtained from our enhanced effective mass approximation (eEMA). Then, we discuss the contributions of individual components and the effect of gate material on it.

3.1 Capacitance versus Gate Voltage

Owing to the voltage dependence of capacitance on both MOS and MOSFET, a more general expression for calculating capacitance is given as

$$C = \left|\frac{dQ_s}{dV_G}\right| \tag{3.1.1}$$

where Q_s denotes the total charge on the semiconductor region. The calculated capacitance versus gate voltage curves are shown in Fig. 3.1.1 and 3.1.2 for unstressed (001) and (110) p-MOSFET. We adopt the effective masses listed in those figures in order to observe the distinctive differences among constant EMA, enhanced EMA, and fully-iterated results. Remarkably, a considerable discrepancy from the constant EMA is revealed in Fig. 3.1.2, due to much heavy (110) *H1* quantization effective mass as shown in Fig. 2.4.4. Therefore, it is found that the effective masses must be treated properly as a consequence of extracting the process parameter. Only with this procedure can the subsequently calculated hole gate direct tunneling current be reasonable. The poly-gate doping, longitudinal compressive stress, and work function

dependence of (001) capacitance are shown theoretically in Fig. 4.3.2 (a), 4.3.3 (a), and 4.3.4 (a) with the enhanced EMA. Low poly-gate doping induces extra poly-gate capacitance in series that will finally cause the overall capacitance decrease, which is clearly demonstrated in Fig. 4.3.2 (a). Fig. 4.3.3 (a) shows the impact of poly-gate doping in weak inversion region, where the threshold voltage shift as the substrate doping and compressive stress increase. Moreover, different gate materials that result in diverse work functions can cause the capacitance shift according to our simulation, which is shown in Fig. 4.3.4 (a).

3.2 Hole Gate Direct Tunneling Current

3.2.1 Physical Model

By referring to [18], the hole current density contributed by the *j*th subband with energy E ranging from $E_{i,v}$, the subband of *v*th bulk band, to infinity can be written as

$$J_{i,v} = \int_{E_{i,v}}^{\infty} q \cdot F_{i,v} \cdot n_{i,v}(E) \cdot T_{i,v}^{WKB}(E) \cdot T_{i,v}^{R}(E) dE \tag{3.2.1.1}$$

$$J_g = \sum_{i,v} J_{i,v} \tag{3.2.1.2}$$

where q denotes the elemental charge, $F_{i,v}$ is impact frequency of hole wave packet on interface, $n_{i,v}(E)$ is inversion carrier density per energy, $T_{i,v}^{WKB}(E)$ is transmission probability through insulator of WKB part, $T_{i,v}^{R}(E)$ is transmission probability through reflection part of insulator and i refers to the subband index while v refers to bulk band index. There are 18 subbands considered in our calculation. These subbands are quantitatively and accurately enough in our simulation. The impact frequency can be described as

$$F_{i,v} = \frac{qE_s}{2}\left(2m_{QN}^{i} E_{i,v}\right)^{-\frac{1}{2}} \tag{3.2.1.3}$$

For the inversion carrier density, we calculate it through

$$n_{i,v} = g_i \frac{m_{DOS}^i}{\pi \hbar^2} k_B T \ln\left(1 + e^{\frac{E_f - E_{i,v}}{kT}}\right) \tag{3.2.1.4}$$

where the degeneracy of ith subband g_i is equal to 2. Among two terms in the transmission probability through oxide layer, the first one is WKB part, which can be modeled as

$$T_{i,v}^{WKB}(E) = \exp\left[-\frac{2}{\hbar}\left|\int_0^{T_{ox}} \sqrt{2m_{oxh}(E - qV(z))}dz\right|\right]$$

$$= \exp\left(\frac{4\sqrt{2m_{oxh}}\left(\varphi_{cath}^{3/2} - \varphi_{an}^{3/2}\right)}{3q\hbar|E_{ox}|}\right) \tag{3.2.1.5}$$

$$\varphi_{cath} = q\chi_h - q|E_{ox}|T_{ox} - E \tag{3.2.1.6}$$

$$\varphi_{an} = q\chi_h - E \tag{3.2.1.7}$$

where φ_{cath} is the barrier height of the tunneling hole with total energy E at cathode side or gate/oxide interface, and φ_{an} is that at anode side or oxide/n-well interface with χ_h is the barrier height of oxide/Si interface.

Another one is $T_{i,v}^R(E)$, which is given as

$$T_{i,v}^R(E) = \mathrm{T}_1^R \times \mathrm{T}_2^R = \frac{4v_{si,\perp}(E)v_{ox}(\varphi_{an})}{v_{si,\perp}^2(E) + v_{ox}^2(\varphi_{an})} \times \frac{4v_{si,\perp}(E + q|E_{ox}|T_{ox})v_{ox}(\varphi_{cath})}{v_{si,\perp}^2(E + q|E_{ox}|T_{ox}) + v_{ox}^2(\varphi_{cath})} \tag{3.2.1.8}$$

where Ts and T_G refer to substrate and gat part, $v_{si,\perp}(E)$ and $v_{si,\perp}(E + q|E_{ox}|T_{ox})$ are the group velocities of the holes incident and leaving oxide, respectively, as in the form:

$$v_{si,\perp}(E) = v_{si,\perp}(z = 0) = \sqrt{\frac{2E_{i,v}}{m_{QN}^i}} \tag{3.2.1.9}$$

Moreover, $v_{ox}(\varphi_{an})$ and $v_{ox}(\varphi_{cath})$ are the magnitudes of the purely imaginary group velocities of holes at the cathode and anode side within the oxide, respectively, as in the form:

$$v_{ox}(E) = \frac{1}{\hbar}\frac{dE_{ox}}{dk_{ox}} = \sqrt{\frac{2E_{ox}}{m_{oxh}}} \quad (3.2.1.10)$$

3.2.2 Simulation Result and Discussion

The calculated hole gate direct tunneling currents for various stress conditions are illustrated in Fig. 3.2.2.1 for both (001) and (110) surfaces. Besides that, the contributions of individual components are given in Fig. 3.2.2.2 to 3.2.2.5. We sum up the inversion carrier density of each subband and average the transmission probability as described below:

$$\langle T_{i,v} \rangle = \frac{\int_{E_{i,v}}^{E_{i,v}+340meV} T_{i,v} f_0(E) dE}{\int_{E_{i,v}}^{E_{i,v}+340meV} f_0(E) dE} \quad (3.2.2.1)$$

where f_0 is the Fermi-Dirac distribution function under equilibrium. Through the experimental fitting as addressed later, we found that for the polysilicon gate as shown in Fig. 3.2.2.6, the value of $m_{poly-Si,\perp}$ associated with the group velocity, Eq.(3.2.10), should be corrected as *0.3* m_0, which is much smaller than the (110) *H1* quantization effective mass. The corrected group velocity is written as below:

$$V_{Si,\perp}^{i,v}(E + q|E_{ox}|T_{ox}) = \sqrt{\frac{2\left(\left(E_{i,v} - E_v^0\right) + q|E_{ox}|T_{ox}\right)}{m_{poly-Si,\perp}^{i}}} \quad (3.2.2.2)$$

where E_{ox} and T_{ox} refer to the oxide field and oxide thickness, respectively. Obviously, the (110) Ig is 6~10 times lower than (001) one. This can be attributed to the reflection part of transmission probability as shown in Fig. 3.2.2.5. Moreover, we have stated that such Ig difference is unnoticeable in metal-gate devices due to negligible reflection term $T_{i,v}^{R}$, which can be easily noticed in Fig. 3.2.2.7. Also shown is the comparison of experimental and calculated hole gate direct tunneling current change versus stress. The bias conditions and process parameters in the calculation are close to

1896

the experiment ones. Apparently, both polysilicon gate and metal gate cases yield satisfactory fitting of strain altered Ig data as published in [2], [5] and [19]. The large slope of (110) Ig change versus stress is mainly due to the sensitive dependence on stress as illustrated in Fig. 3.2.2.2 to 3.2.2.5. In Fig. 3.2.2.7, we add the (110) case of no correction for the effective mass in the reflection term. There occurs a large discrepancy, unless a correction on $m_{poly-Si,\perp}$ has been made. This trend remains the same even when we extend our simulation to higher stress of up to -3GPa, which is shown in Fig. 3.2.2.8. In addition, this is the first time to demonstrate that at higher stresses, the rate of Ig change gets slow for both (100) and (110) cases. In order to corroborate this projection, we again add into the inset of the figure the comparison of corresponding mobility enhancement values with those of Packan *et. al* [20]. Our simulation results are obtained through sophisticated simulations in Fig. 1.1 in combination with a Kubo-Greenwood formula. A good agreement is reached in our simulation for both (001) and (110) surface. We have also produced a reasonable fitting of available experimental Ig-Vg curves in (110) sidewall-surface p-FinFETs with and without the stress from [2], which is shown in Fig. 3.2.2.9. The hole gate direct tunneling current that dominated in (110) sidewall of FinFET was well described by our simulation. Moreover, calculated hole gate direct tunneling currents for both (001) and (110) p-MOSFETs with polysilicon, FUSI and metal gates are illustrated in Fig. 3.2.2.10 and Fig. 3.2.2.11. Fig 3.2.2.12 shows the comparison of hole gate direct tunneling current change versus stress for both (001) and (110) p-MOSFETs among polysilicon, FUSI and metal gates. Clearly, FUSI gates have outstanding control over hole gate direct tunneling current. More specific discussions about FUSI gate will be given in next chapter.

Chapter 4

Individual Contributions to 40% Gate Current Reduction in FUSI Gate Strained (001) p-MOSFETs

4.1 Introduction

Although use of metal gate can eliminate poly-depletion effect, some challenging issues exist in terms of the process integration and the work function control. The key requirement for work function control is to meet the threshold voltage specifications for each application. Fortunately, the fully silicided (FUSI) gate whose property lies between polysilicon gate and metal gate could serve as an alternative to metal gates due to the advantages of good process compatibility with silicon [21], threshold voltage control [22],[23], and even the suppression of hole gate direct tunneling current [24]. Our main purpose in this chapter is to decouple the contributions of the observed 40% gate current reduction in FUSI-gate (001) p-MOSFET with respect to polysilicon one [24]. Initially, the nominal process parameters are obtained by both the gate capacitance Cg fitting and gate current Ig fitting. Then, we separated out individual contributions due to (i) gate work function WF shift; (ii) elimination of poly depletion; (iii) channel stress change, (iv) T_R part missing in FUSI gate, and (v) V_{th} roll-off in FUSI gate, all achieved by means of our eEMA algorithm. The extracted work function values will be justified.

4.2 Parameter Extraction

With the proposed eEMA, the nominal process parameters for both polysilicon gate and FUSI gate p-MOSFETs are obtained as shown in Fig. 4.2.1 and Fig. 4.2.2. For CV measurement, the large dimension devices are selected to ensure the quality of the

extracted parameters. On the other hand, samples with small dimension are preferred for the investigation of gate leakage current. The extracted process parameters are SiON effective oxide thickness $\mathrm{EOT} = 1.32\mathrm{nm}$, n-type substrate doping concentration $N_{sub} = 1.6 \times 10^{18} cm^{-3}$, permittivity of SiON $\varepsilon_{SiON} = 5\varepsilon_0$, the SiON/Si barrier height $q\chi_h = 3.8\mathrm{eV}$, effective electron mass $m_{SiON} = 0.27m_0$, the p^+ polysilicon dopant concentration and work function for polysilicon gate $N_{poly} = 6.5 \times 10^{19} cm^{-3}$ and $\mathrm{WF} = 5.17\mathrm{eV}$, respectively. Particularly, the work function for FUSI gate was found to be 5.013 eV.

4.3 Simulation Result and Discussion

The gate capacitance-voltage measurement is done using a large device sample. Thus, we can suppose no additional longitudinal or transverse stress induced by S/D region, STI or capping layers. However, we found that FUSI gates impose an extra stress of around -460 MPa on the underlying p-MOSFET channel region, which can be directly confirmed by C-V curve in Fig. 4.3.1. We have produced more consistent fittings in weak inversion region if longitudinal channel stress -460 MPa is taken into account in FUSI gates. In contrast to C-V counterpart, the measurement of Ig is done under small device, the corresponding longitudinal channel stress for polysilicon gate and FUSI gate are -1.83 and -2.29 GPa, respectively, as revealed from TCAD results in [24]. Fig. 4.3.2 shows the influence of polysilicon dopant concentration on both CV and Ig. For dopant concentration as high as $1 \times 10^{23} cm^{-3}$, the strong inversion regions in CV behave similarly as metal gate, but the Ig acts differently due to negligible transmission probability across reflection part of the insulator and work function shift. Besides, around 6% of Ig difference occurs between -1.83 GPa and -2.29 GPa, which is too small to be observed even in the log-scale, as shown in Fig. 4.3.3. This phenomenon is quite consistent with our simulation result in previous chapter, Fig.

3.3.2.8, where the rate of Ig change gets slow at higher stress. Moreover, C-V and Ig-Vg curves both shift tremendously due to various work functions, as shown in Fig. 4.3.4. The carrier reflection part of transmission probability through insulator T_R is one of the important issues in FUSI gate that should be discussed. As revealed in Fig. 4.2.1, we find that the T_R part may not exist in FUSI gate as like the metal counterpart. The similar discovery in metal gate is mentioned by Li, et al [25]. Finally, the Ig defference between polysilicon gate p-MOSFETs (-1.83 GPa) and fully-silicided (FUSI) ones (-2.29 GPa) can be quantitatively interpreted, as depicted in Fig. 4.3.5: most of the hole gate direct tunneling current changes are due to gate materials through either WF shift (-95%) or poly depletion (+62%), T_R part missing(-26%), +24% for V_{th} roll-off in FUSI gate (0.1 Volt, while having only -6% change from stress. We further demonstrate that the overall Ig change between polysilicon and FUSI gates is around 41% (from 8.2 to 4.8 A/cm^2) if we sum all the contributions. The comparisons of work function of Ni FUSI with those of [26] and [27] are shown in Fig. 4.3.6. It is worth noticing that the addition of dopants such as B and P to polysilicon before silicidation may cause significant shifts in the work function of silicided [27], especially when the silicide is Si-richer. In contrast, the change is negligible in Ni-rich silicides. As a result, we strongly believe that the extracted work function from our eEMA is reasonable.

Chapter 5
Conclusion

We have proposed the enhanced version of effective mass approximation algorithm (eEMA). The validity of eEMA has been confirmed through the comparison between the conventional EMA, the enhanced EMA and the sophisticated six-band k.p. We have shown that conventional hole effective masses may lead to unacceptable error. Only with bias and stress dependencies taken into account can accurate calculation of gate capacitance and hole gate direct tunneling current be obtained. The hole gate direct tunneling current in both (001) and (110) strained p-MOSFETs have already been simulated under various longitudinal compressive stress. Moreover, the contributions of hole gate direct tunneling current have been distinguished and have been further discussed, especially the transmission probability of across reflection part of the insulator due to its substantial impact on resulting gate current. Satisfactory agreements could be achieved as compared with existing experimental data of strain-induced gate direct tunneling current change under polysilicon and metal gates. In addition, the simulated result from eEMA has successfully fitted the experimental data of p-FinFETs with and without stress. Finally, we have demonstrated the potential application on FUSI gate case in terms of individual contributions of work function shift, polysilicon depletion elimination, and increased channel compressive stress magnitude.

References

[1] L. F. Register, E. Rosenbaum, and K. Yang, "Analytic model for direct tunneling current in polycrystalline silicon-gatemetal–oxide–semiconductor devices," *Appl. Phys. Lett,* vol. **74**, no. 3, pp. 457-459, Jan. 1999.

[2] M. Saitoh, A. Kaneko, K. Okano, T. Kinoshita, S. Inaba, Y. Toyoshima, and K. Uchida, "Three-dimensional stress engineering in FinFETs for mobility/on-current enhancement and gate current reduction," *in Symposium on VLSI Technology,* pp. 18-19, 2008.

[3] T. Low, Y. T. Hou, and M. F. Li, "Improved one-band self-consistent effective mass methods for hole quantization in p-MOSFET," *IEEE Trans. Electron Devices*, vol. **50**, no. 5, pp. 1284-1289, May 2003.

[4] M. J. Chen, C. C. Lee, and K. H. Cheng, "Hole effective masses as a booster of self-consistent six-band k·p simulation in Inversion layers of pMOSFETs," *IEEE Trans. Electron Devices*, vol. **58**, no. 4, pp. 931-937, April 2011.

[5] S. E. Thompson, G. Sun, Y. S. Choi, and T. Nishida, "Uniaxial-process-induced strained-Si: extending the CMOS roadmap," *IEEE Trans. Electron Devices*, vol. **53**, no. 5, pp. 1010-1019, May 2006.

[6] M. Saitoh, S. Kobayashi, and K. Uchida, "Physical understanding of fundamental properties of Si (110) pMOSFETs inversion-layer capacitance, mobility universality, and uniaxial stress effects," *in IEDM Tech. Dig.,* pp. 711-714, 2007.

[7] Y. Sun, S. E. Thompson, and T. Nishida, "Physics of strain effects in semiconductors and metal-oxide-semiconductor field-effect transistors," *J. Appl. Phys.*, vol. **101**, no. 10, p. 104503, May 2007.

[8] Roy R. Craig, Jr., Mechanics of Materials, second edition, John Wiley & Sons inc., 1999.

[9] Wikipedia (http://en.wikipedia.org/wiki/Main_Page)

[10] Fusahito Yoshida, "Fundamentals of elastic plastic mechanics," KYOROTSU SHUPPAN Co., Ltd., 1997.

[11] H. A. Reuda, "Modeling of mechanical stress in silicon isolation technology and its influence on device characteristics," dissertation of degree of doctor of philosophy, university of Florida, 1999.

[12] M. V. Fischetti, Z. Ren, P. M. Solomon, M. Yang, and K. Rim, "Six-band $k \cdot p$ calculation of the hole mobility in silicon inversion layers: Dependence on surface orientation, strain, and silicon thickness," *J. Appl. Phys.*, vol. **94**, no. 2, pp. 1079-1095, Jul. 2003.

[13] Frank Stern, "Self-consistent results for n-type Si inversion layers," *Phys. Rev. B*, vol. **5**, no. 12, pp. 4891-4899, June 1972.

[14] W. J. Fan, M. F. Li, T. C. Chong, and J. B. Xia, "Valence hole subbands and optical gain spectra of $GaN/Ga_{1-x}Al_xN$ strained quantum wells," *J. Appl. Phys.*, vol. **80**, pp. 3471-3478, Sept. 1996.

[15] Schred. [Online]. Available:http://nanohub.org/resources/schred

[16] D. Vasileska, D. K. Schroder, and D.K. Ferry, "Scaled silicon MOSFETs: degradation of the total gate capacitance," IEEE Trans. Electron Devices, vol. 44, no.4, pp.584-587, Apr. 1997.

[17] S. Takagi, M. Takayanagi, and A. Toriumi, "Characterization of inversion-layer capacitance of holes in Si MOSFET's," *IEEE Trans. Electron Devices*, vol. 46, pp. 1446-1450, July 1999.

[18] K. N. Yang, H. T. Huang, M. C. Chang, C. M. Chu, Y. S. Chen, M. J. Chen, Y. M. Lin, M. C. Yu, S. M. Jang, D. C. H. Yu, and M. S. Liang, "A physical model for hole direct tunneling current in p+ poly-gate pMOSFETs with ultrathin gate oxides," *IEEE Trans. Electron Devices*, vol. **47**, no. 11, pp. 2161-2166, Nov. 2000.

1896

[19] X. Yang, J. Lim, G. Sun, K. Wu, T. Nishida, and S. E. Thompson, "Strain-induced changes in the gate tunneling currents in p-channel metal-oxide-semiconductor field-effect transistors," *Appl. Phys. Lett.*, vol. **88**, pp. 0521081-0521083, Jan. 2006.

[20] P. Packan, S. Cea, H. Deshpande, T. Ghani, M. Giles, O. Golonzka, M. Hattendorf, R. Kotlyar, K. Kuhn, A. Murthy, P. Ranade, L. Shifren, C. Weber, and K. Zawadzki, "High performance Hi-K + metal gate strain enhanced transistors on (110) silicon," in *IEDM Tech. Dig.*, 2008, pp. 63-66.

[21] Hidenobu Fukutome, Kimihiko Hosaka, Kazuo Kawamura, Hiroyuki Ohta, Yasunori Uchino, Shinichi Akiyama, and Takayuki Aoyama, "Sub-30-nm FUSI CMOS transistors fabricated by simple method without additional CMP process," *IEEE Trans. Electron Devices*, vol. **29**, no. 7, pp. 765-767, July 2008

[22] E. P. Gusev, C. Cabral, B. Linder, Y. H. Kim, K. Maitra, E. Cartier, H. Nayfeh, R. Amos, G. Biery, N. Bojarczuk, A. Callegari, R. Carruthers, S. A. Chohen, M. Copel, S. Fang, M. Frank, S. Guha, M. Gribelyuk, P. Jamison, R. Janny, M. Ieong, J. Kedzierski, P. Kozlowski, V. Ku, D. Lacey, D. Latulipe, V. Narayanan, H. Ng, P. Nguyen, J. Newbury, V. Paruchuir, R. Rengarajan, G. Shahidi, A. Steegen, M. Steen, S. Zafar, and Y. Zhang, "Advanded gated stacks with fully silicided (FUSI) gates and high-κ dielectrics: enhanced performance at reduced gate leakage," in *IEDM Tech. Dig.*, pp. 79–83, 2004.

[23] A. Lauwers, A. Veloso, T. Hoffmann, M. J. H. van Dal1, C. Vrancken, S. Brus, S. Locorotondo, J.-F. de Marneffe, B. Sijmus, S. Kubicek, T. Chiarella, M. A. Pawlak, K. Opsomer, M. Niwa, R. Mitsuhashi2, K. G. Anil, H.Y. Yu, C. Demeurisse, R. Verbeeck, M. de Potter, P. Absil, K. Maex, M. Jurczak, S. Biesemans and J. A. Kittl, "CMOS Integration of dual work function phase controlled Ni FUSI with simultaneous silicidation of NMOS (NiSi) and PMOS (Ni-rich silicide) gates on HfSiON" in *IEDM Tech. Dig.*, pp. 661-664, 2005.

[24] D. W. Lin, M. Wang, M. L. Cheng, Y. M. Sheu, B. Tarng, C. M. Chu, C. W. Nieh, C. P. Lo, W. C. Tsai, R. Lin, S. W. Wang, K. L. Cheng, C. M. Wu, M. T. Lei C. C. Wu, C. H. Diaz, and M. J. Chen, "A millisecond-anneal-assisted selective fully silicided (FUSI) gate process," *IEEE Electron Devices Letter*, vol. **29**, no. 9, pp. 998-1000, Sept. 2008.

[25] F. Li, S. P. Mudanai, Y. Y. Fan, L. F. Register, and S. K. Banerjee, "Physically based quantum-mechanical compact model of MOS devices substrate-injected tunneling current through ultrathin (EOT~1nm) SiO2 and high-κ gate stacks," *IEEE Trans. Electron Devices*, vol. 53, no. 5, pp. 1096-1106, May 2006.

[26] T. Nakayama, K. Kakushima, O. Nakatsuka, Y. Machida, S. Sotome, T. Matsuki, K. Ohmori, H. Iwai2, S. Zaima, T. Chikyow, K. Shiraishi, and K. Yamada: "Theory of workfunction control of silicides by doping for future Si-nano-devices based on fundamental Physics of why silicides exist in nature," *IEDM*, pp. 375-378, 2010.

[27] J. A. Kittl,a_ B. J. O'Sullivan, V. S. Kaushik, A. Lauwers, M. A. Pawlak, T. Hoffmann, C. Demeurisse, C. Vrancken, A. Veloso, P. Absil, and S. Biesemans, "Work function of Ni3Si2 on HfSi*x*O*y* and SiO2 and its implication for Ni fully silicided gate applications," *Appl. Phys. Lett.*, vol. 90, 032103, Jan. 2007.

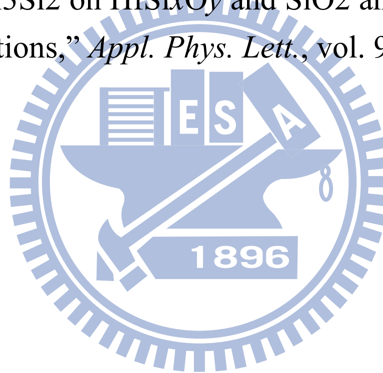

Gate Material	N_{sub} (cm^{-3})	N_{poly} (cm^{-3})	EOT (nm)	Long. Stress σ (GPa)	m_{SiON} (m_0)	Barrier Height (eV)	ε_{SiON}	WF (eV)
P^+ Poly	1.6×10^{18}	6.5×10^{19}	1.32	-1.83	0.27	3.8	5	5.17
FUSI		1×10^{23}		-2.29				5.013

Table I The extracted parameters for Fig. 4.2.1 and 4.2.2.

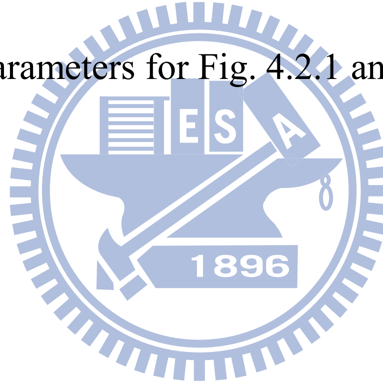

Parameter	This Work	Parameter	This Work
γ_1	4.285	Optical energy $\hbar$ (meV)	61.2
γ_2	0.339	Crystal density ρ (g/cm^3)	2.329
γ_3	1.446	Sound velocity u_l (m/s)	9040
a (eV)	2.46	Optical phonons D_{op} (10^8 eV/cm)	6
b (eV)	-2.1	Acoustic phonons D_{ac} (eV)	4.5
d (eV)	-4.8	Surface Roughness Amplitude Λ (10^{-8} cm)	2.6
Δ (eV)	0.044	The Correlation Length of Surface Roughness Δ (10^{-8} cm)	0.5
$S_{11}(10^{-12}m^2/N)$	7.68		
$S_{12}(10^{-12}m^2/N)$	-2.14		
$S_{44}(10^{-12}m^2/N)$	12.6		

Table II. Hole band, hole scattering and physical parameters used in this work.

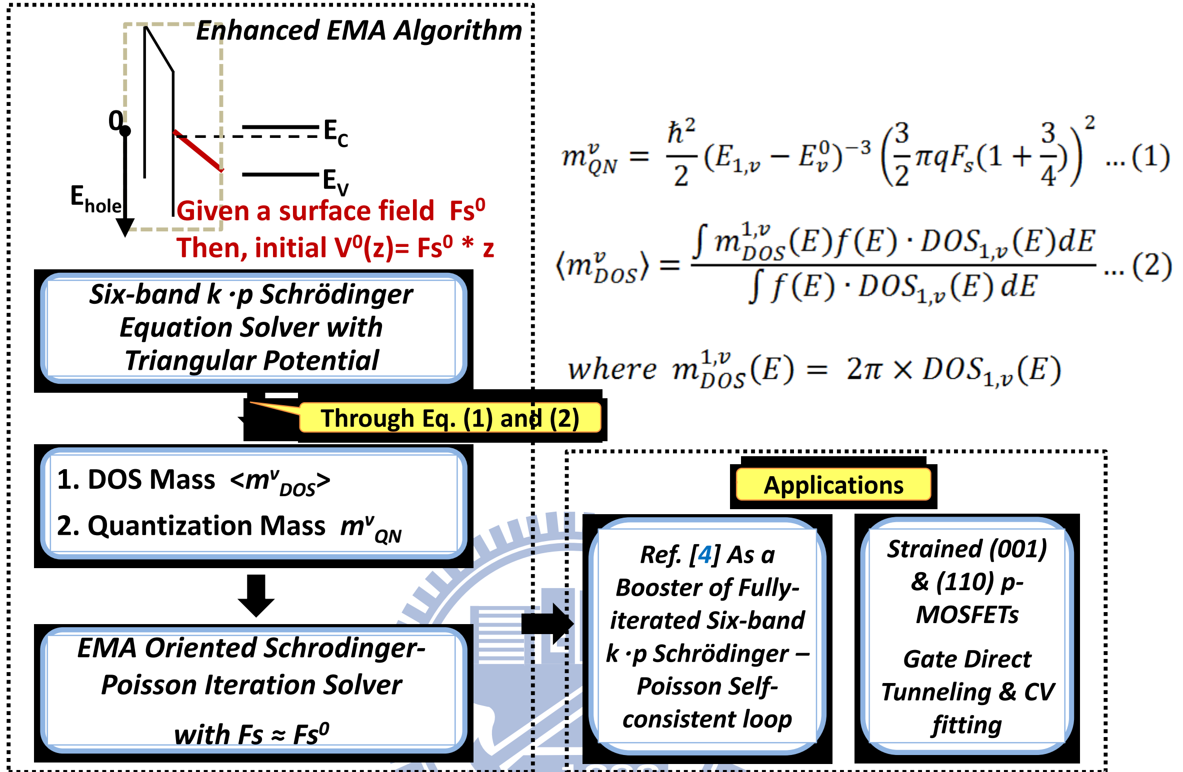

Fig. 2.1The flowchart of our enhanced EMA algorithm. In the inserted equations, $E_{1,v}$ is the first subband of the vth bulk band E_v^0, and $DOS_{1,v}(E)$ is the density-of-states function for $E_{1,v}$. F_s is the surface field, q is the free electron charge, and $f(E)$ is the Fermi-Dirac distribution.

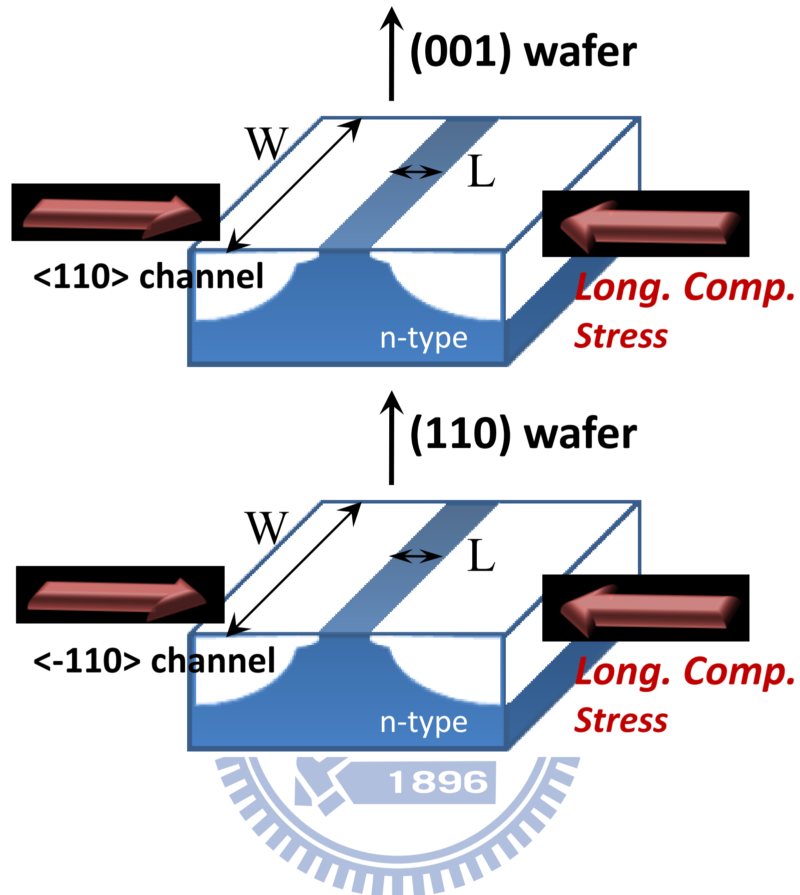

Fig. 2.2 The device structures for (001) and (110) p-MOSFETs. The channel direction and applied stress direction are clarified. Here, only the favorable longitudinal compressive stress is under study.

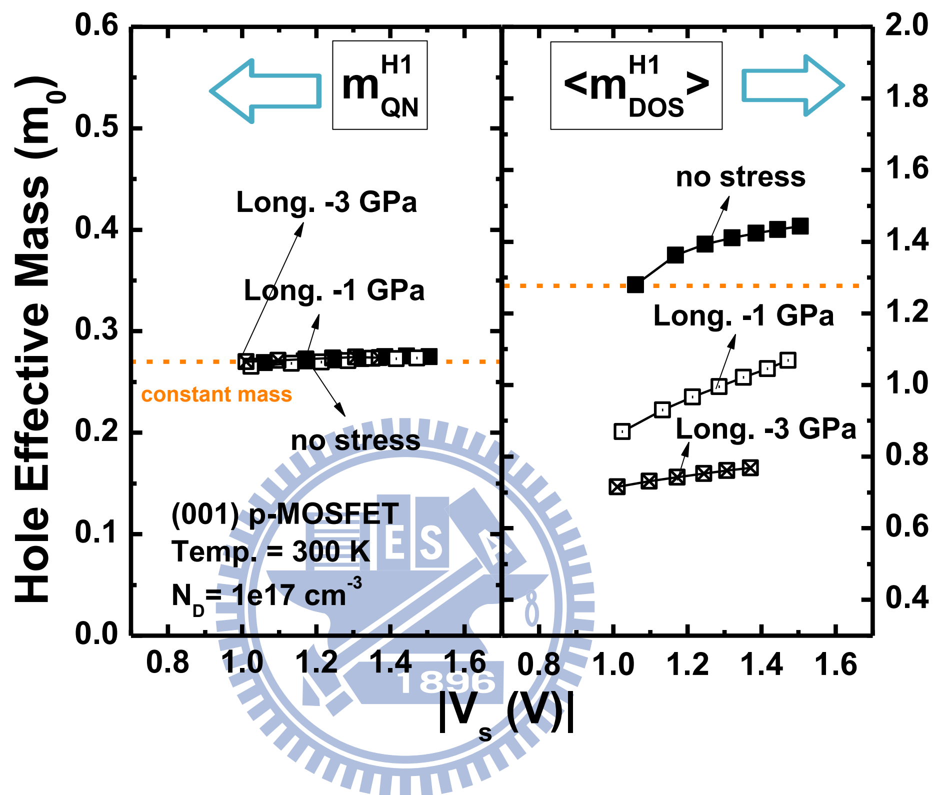

Fig. 2.4.1 The resulting (001) effective masses for H1 bulk band versus surface bending. The heavy, light, and split-off holes, for each subband energy, are mixed due to the coupling effect from the surface quantum confinement or the strain effect [7]. Therefore, we group the subband energies mainly according to the three lowest bulk bands, E_1^0(H1), E_2^0(H2), and E_3^0(H3).

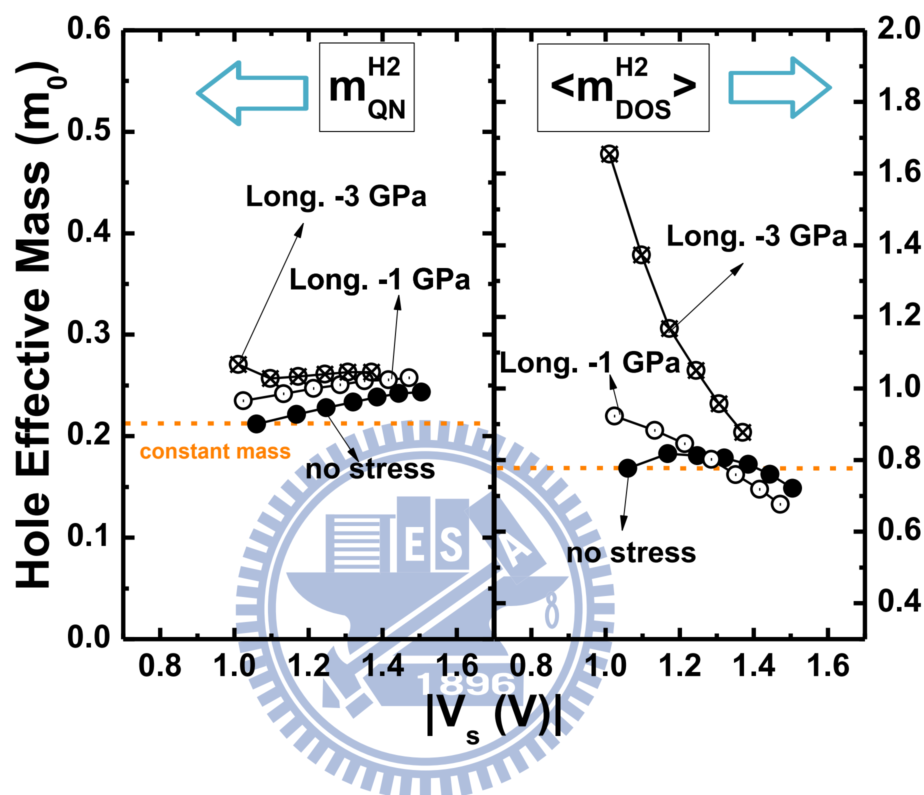

Fig. 2.4.2 The resulting (001) effective masses for H2 bulk band. The orange dashed lines refer to the constant effective masses as in unstressed conditions.

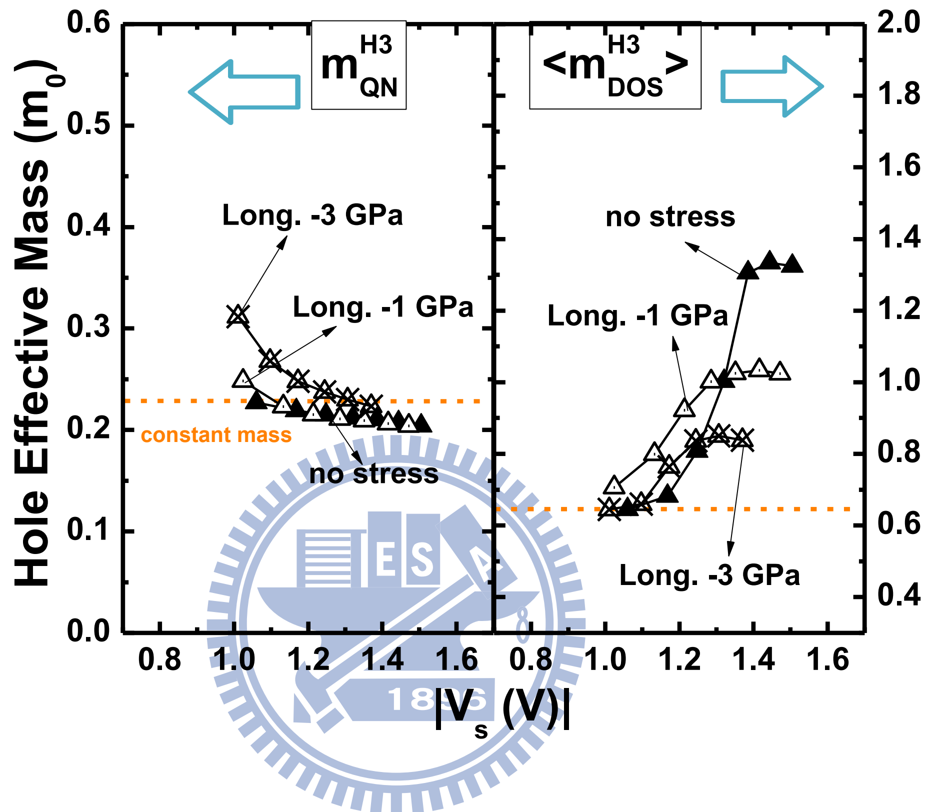

Fig. 2.4.3 The resulting (001) effective masses for H3 bulk band.

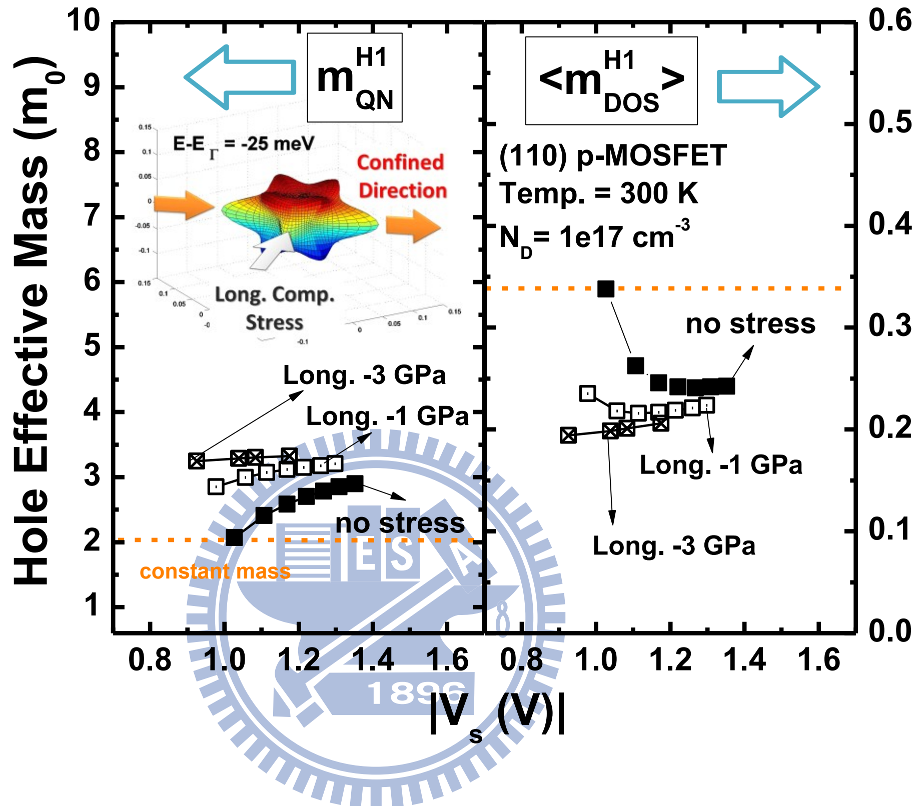

Fig. 2.4.4 The resulting (110) effective masses for H1 bulk band. Only H1 and H2 bulk bands are shown in (110) case here because of their high occupation in the subband energies. Note that (110) m_{QN}^{H1} is stress sensitive.

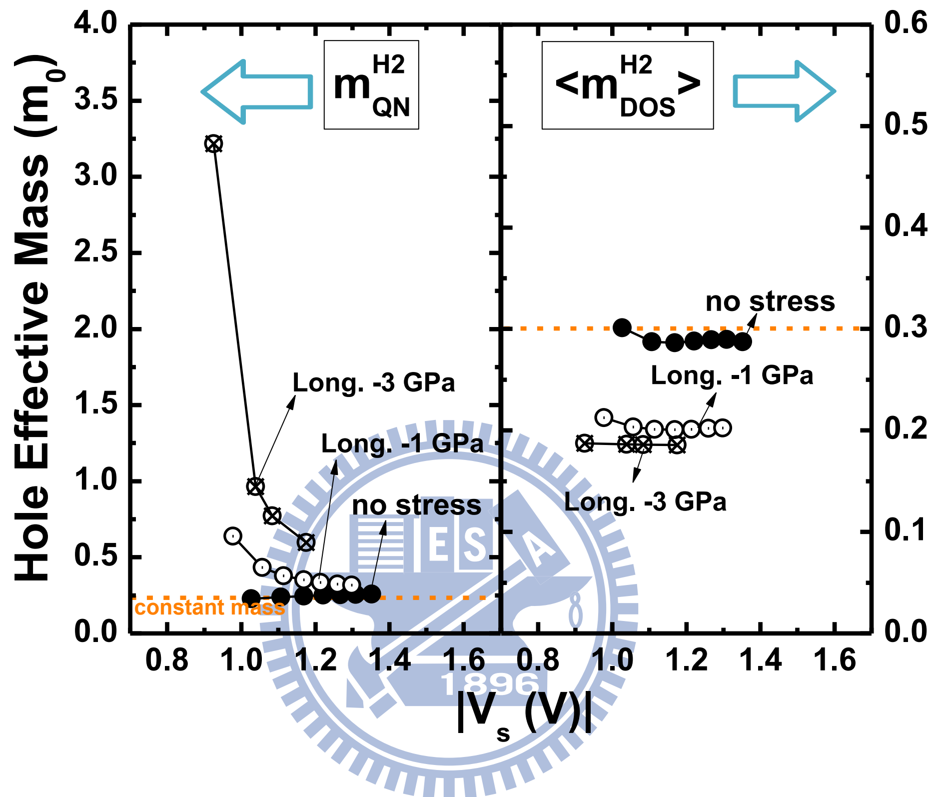

Fig. 2.4.5 The resulting (110) effective masses for H2 bulk band.

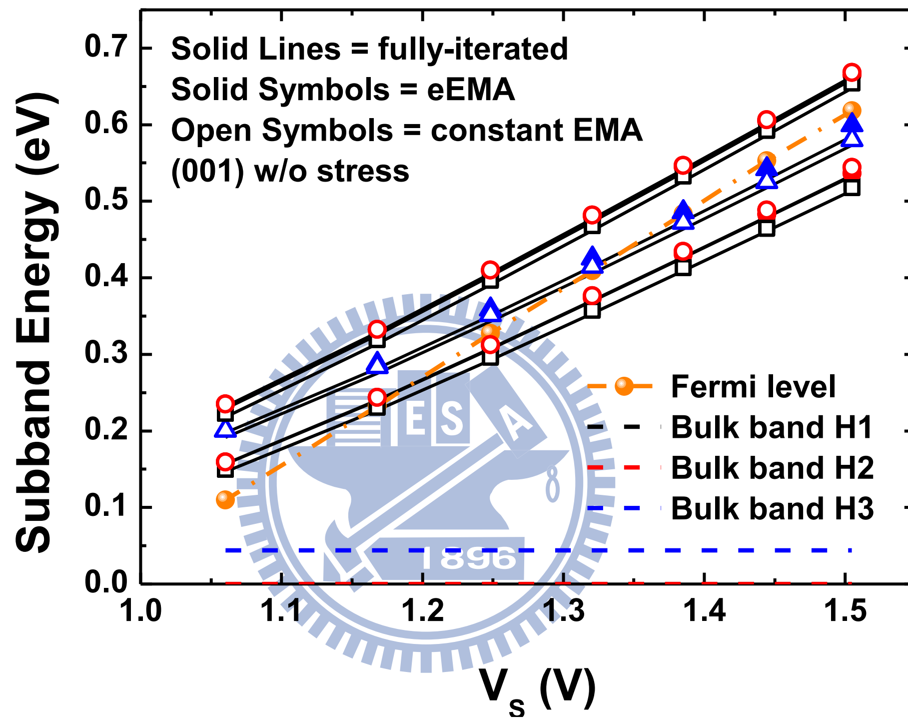

Fig. 2.4.6 The comparison of subband energy of (001) without stress among fully-iterated, eEMA and constant EMA.

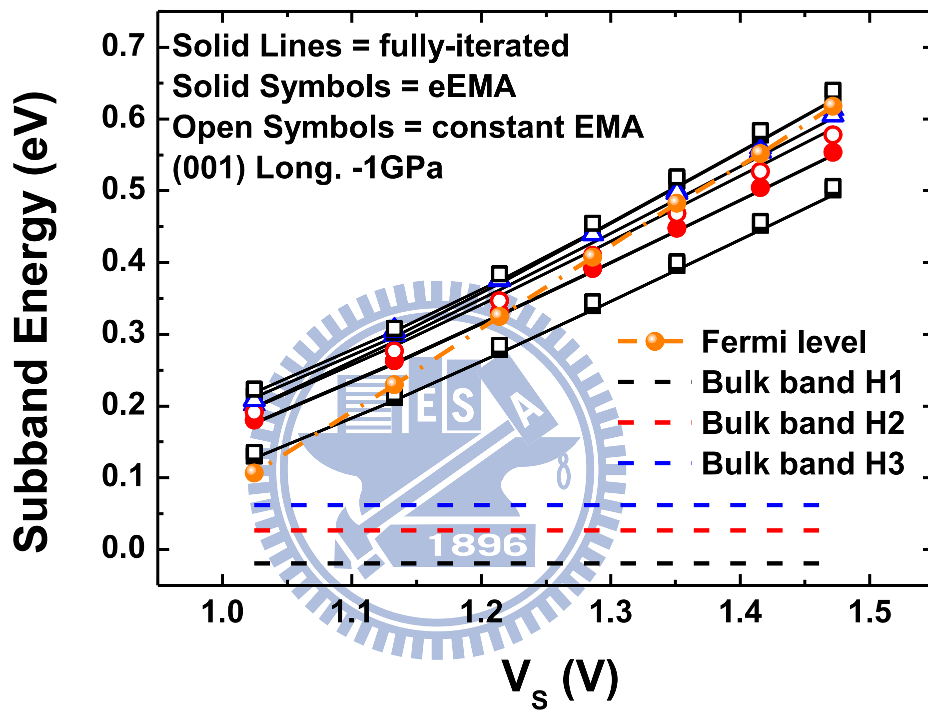

Fig. 2.4.7 The comparison of subband energy of (001) under longitudinal compressive stress 1 GPa among fully-iterated, eEMA and constant EMA.

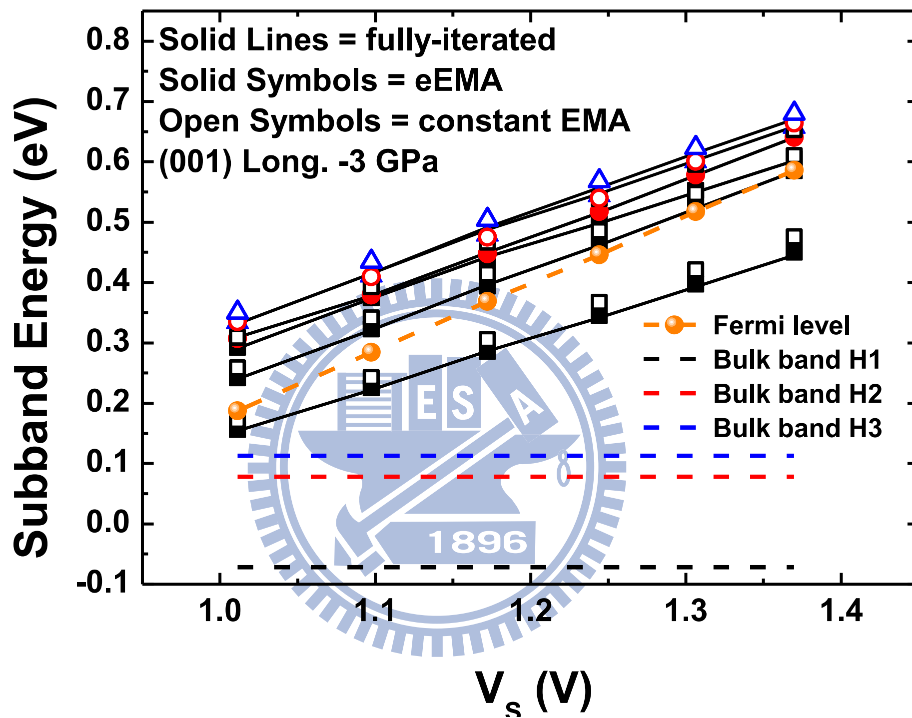

Fig 2.4.8 The comparison of subband energy of (001) under longitudinal compressive stress 3 GPa among fully-iterated, eEMA and constant EMA.

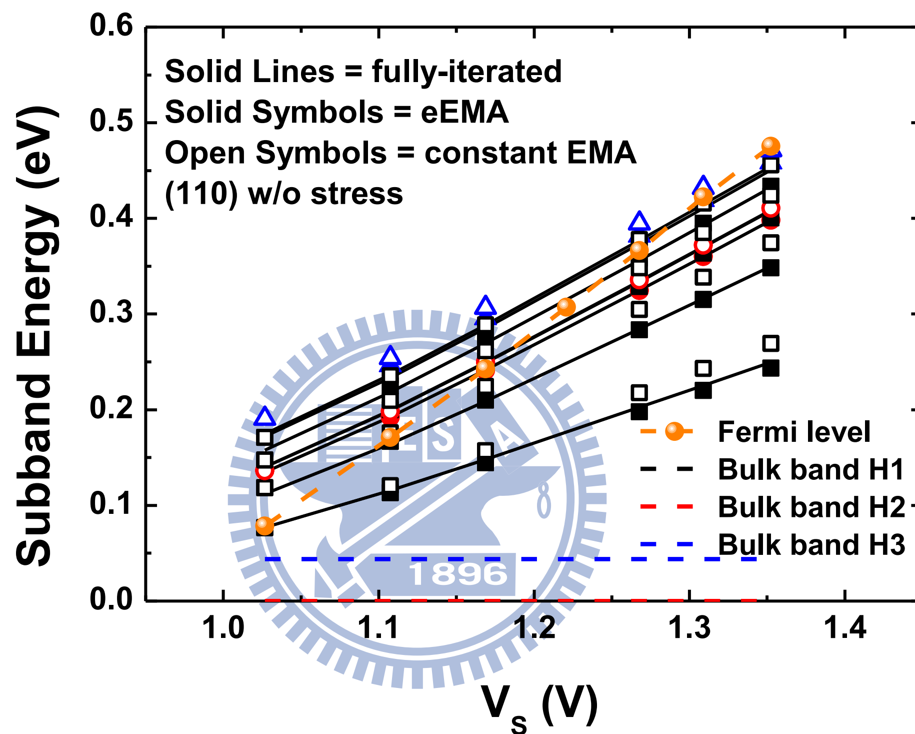

Fig. 2.4.9 The comparison of subband energy of (110) without stress among fully-iterated, eEMA and constant EMA.

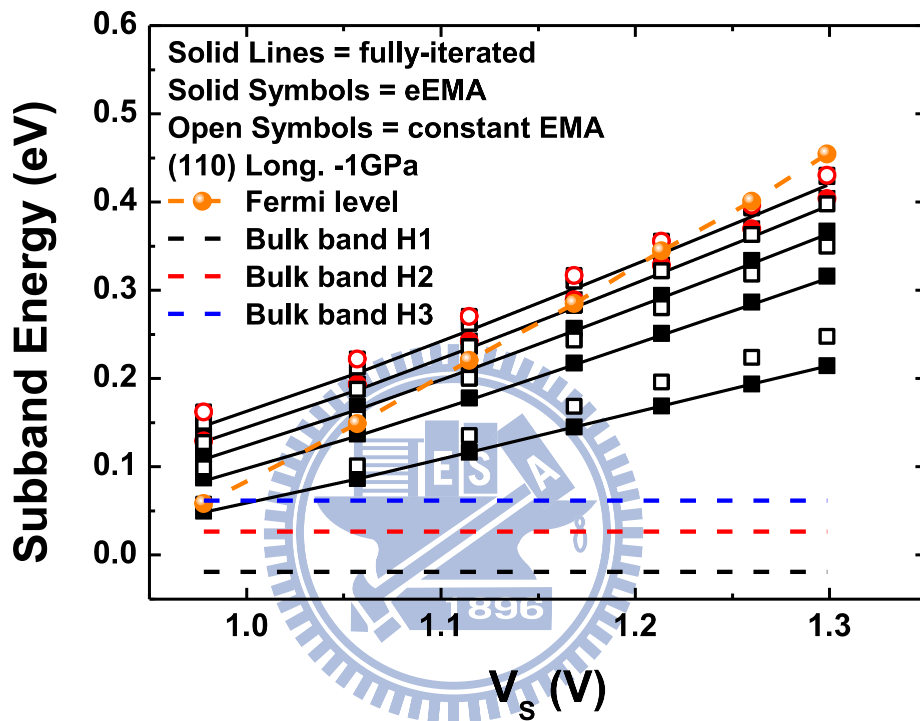

Fig. 2.4.10 The comparison of subband energy of (110) under longitudinal compressive stress 1 GPa among fully-iterated, eEMA and constant EMA.

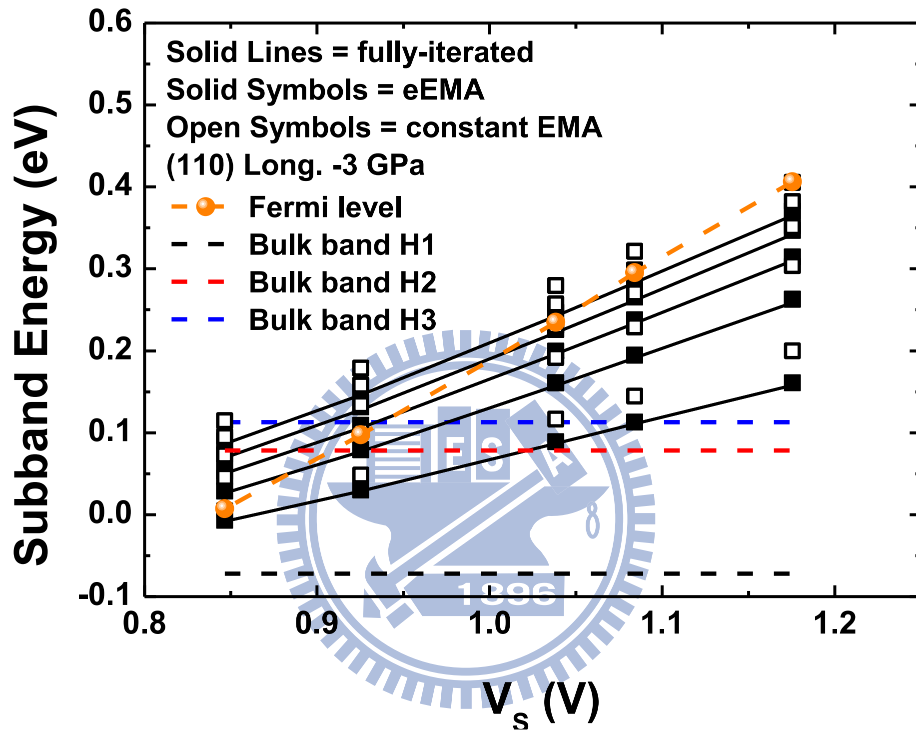

Fig. 2.4.11 The comparison of subband energy of (110) under longitudinal compressive stress 3 GPa among fully-iterated, eEMA and constant EMA.

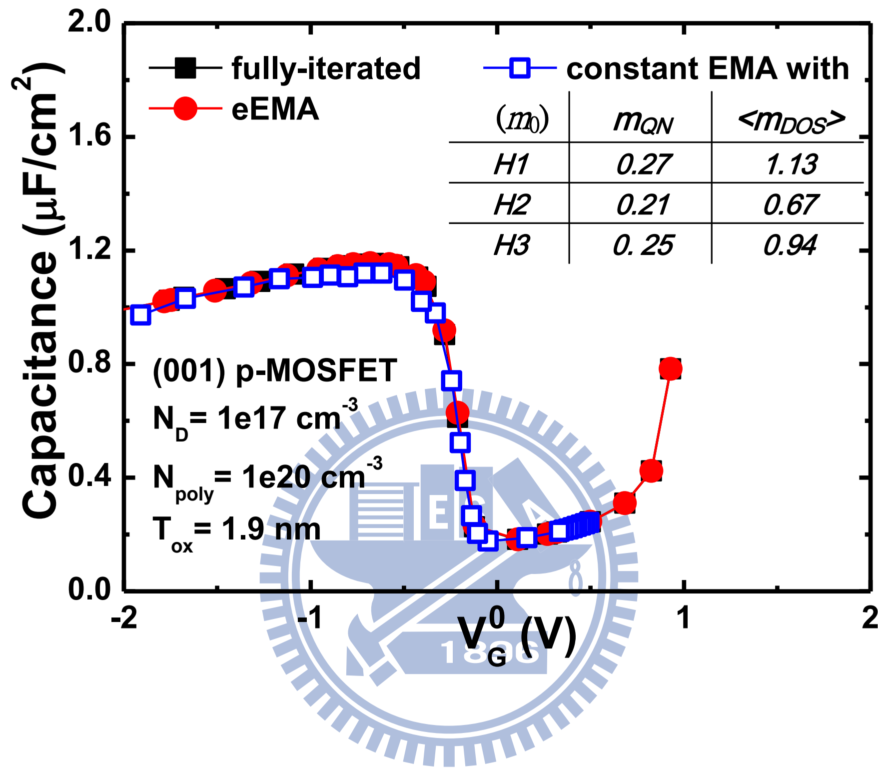

Fig. 3.1.1 The comparison of calculated non-stress (001) gate capacitance versus gate voltage from the constant EMA and enhanced EMA with the sophisticated six-band k·p results.

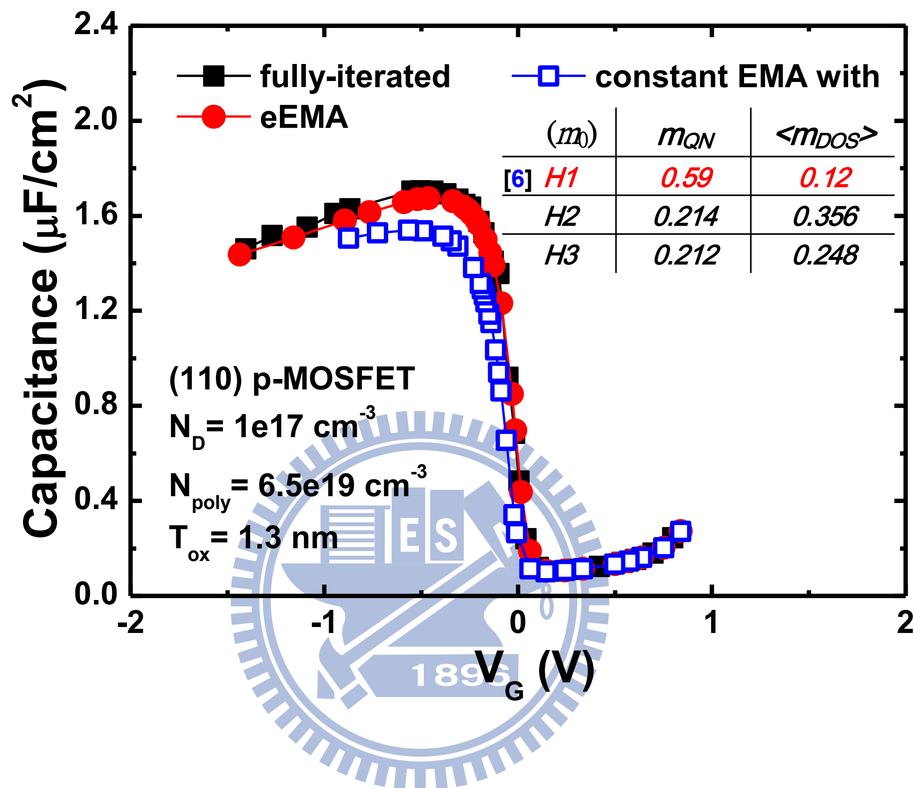

Fig. 3.1.2 The comparison of calculated non-stress (110) gate capacitance versus gate voltage from the constant EMA and enhanced EMA with the sophisticated six-band k·p results.

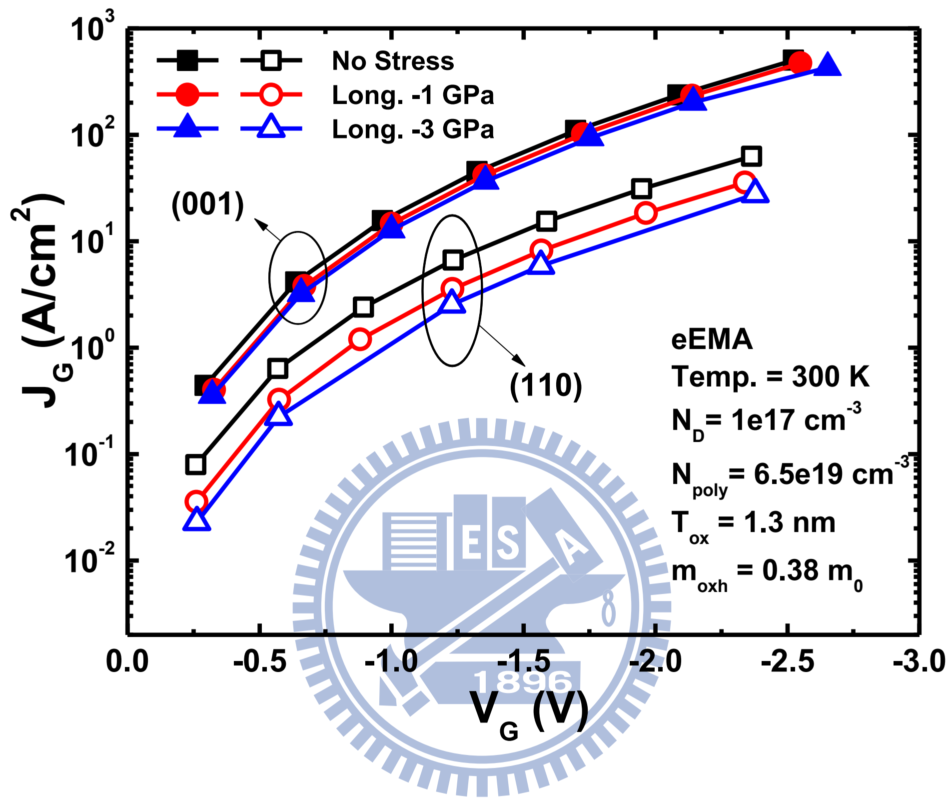

Fig. 3.2.2.1 The calculated hole gate direct tunneling current density for (001) and (110) p-MOSFETs under the longitudinal stress conditions of 0, -1, and -3 GPa. It is contributed by four parts: 1) $F_{i,v}$ impact frequency of hole wave packet on interface, 2) $n_{i,v}(E)$inversion carrier density per energy, 3) $T_{i,v}^{WKB}(E)$ WKB part of transmission probability through insulator, and 4) $T_{i,v}^{R}(E)$ reflection part of transmission probability through insulator.

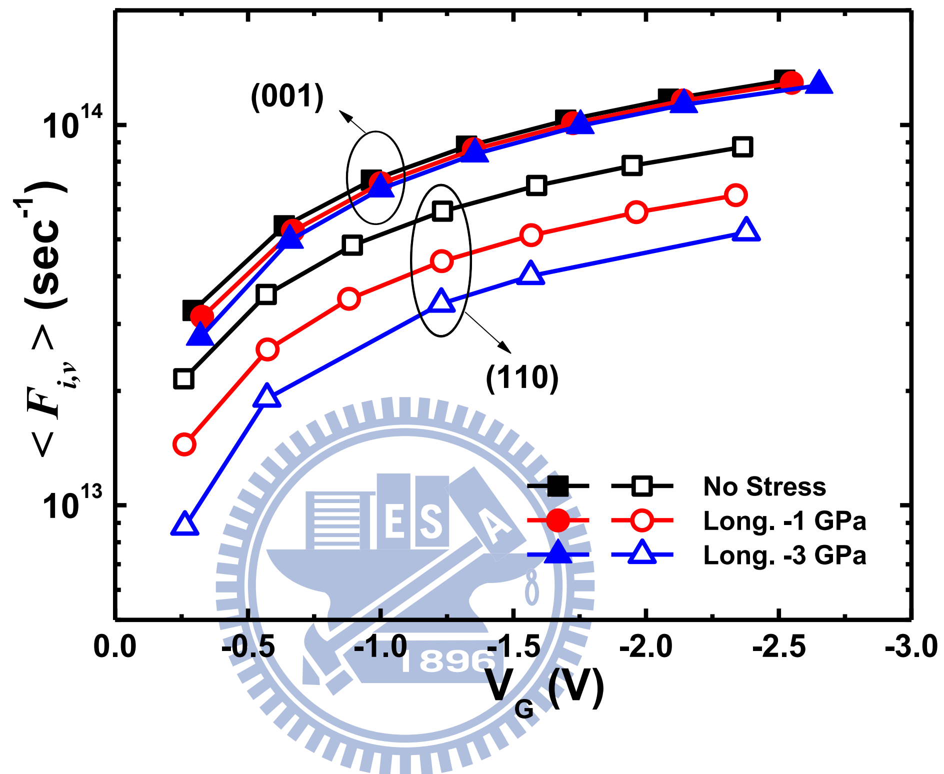

Fig. 3.2.2.2 The contribution of the averaged impact frequency of hole wave packet on interface for (001) and (110) p-MOSFETs under the longitudinal stress conditions of 0, -1, and -3 GPa.

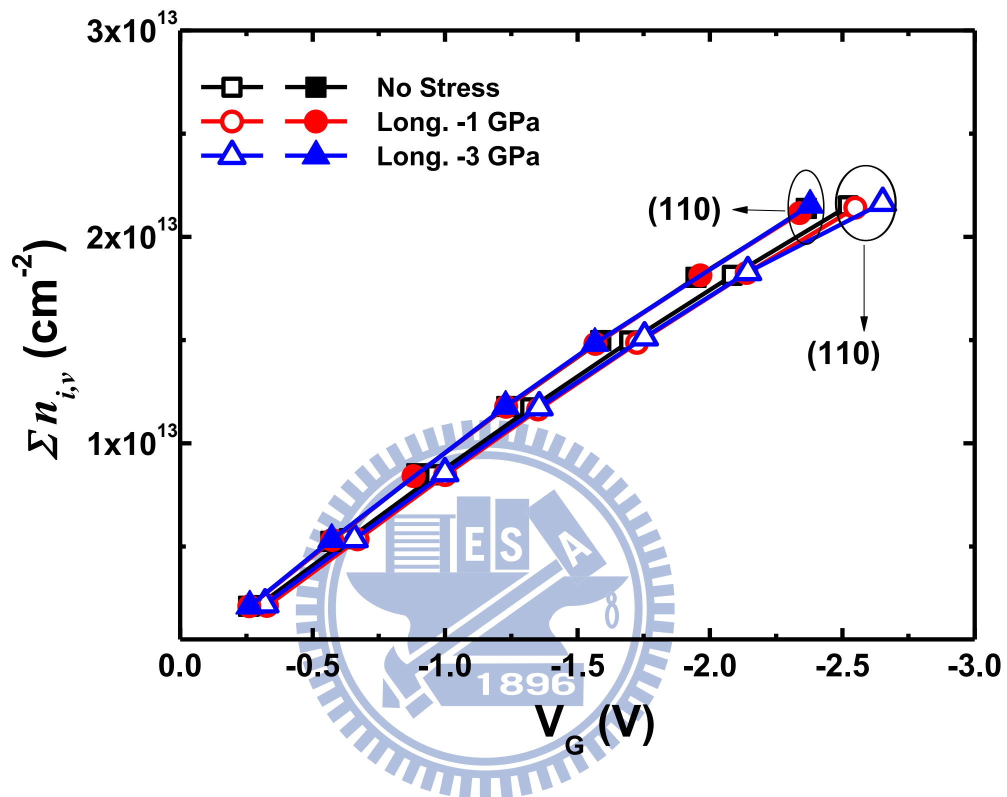

Fig. 3.2.2.3 The contributions of the total inversion carrier density for (001) and (110) p-MOSFETs under the longitudinal stress conditions of 0, -1, and -3 GPa.

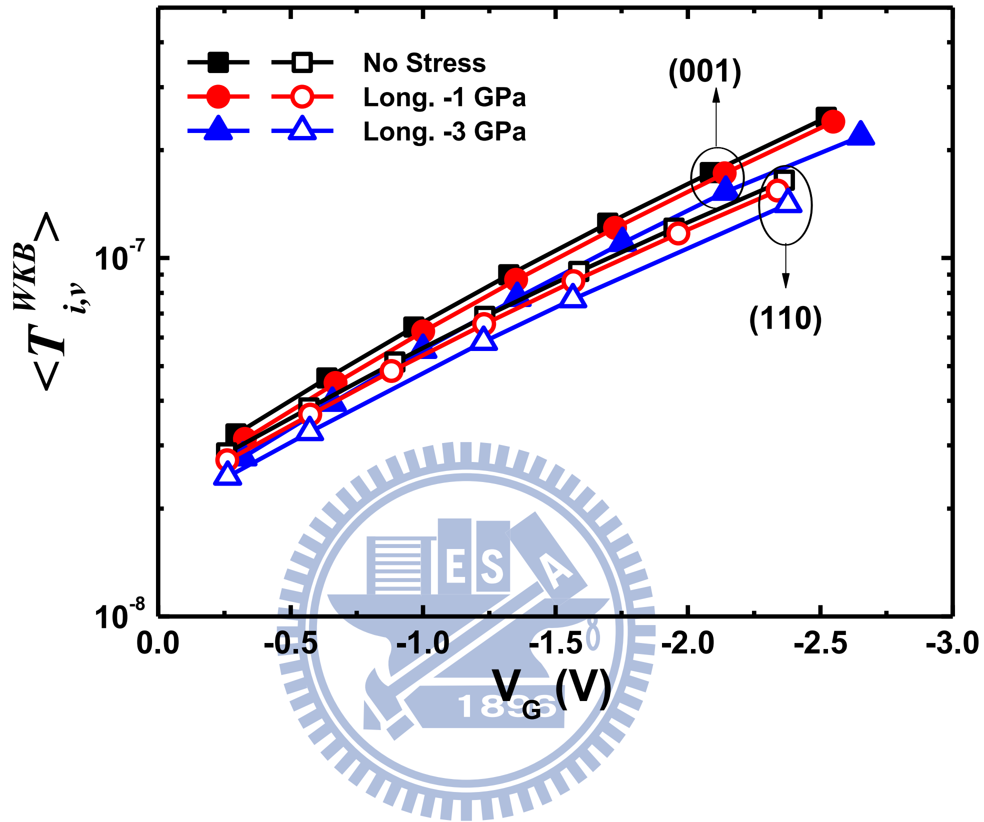

Fig. 3.2.2.4 The contributions of the average WKB transmission probability through insulator for (001) and (110) p-MOSFETs under the longitudinal stress conditions of 0, -1, and -3 GPa.

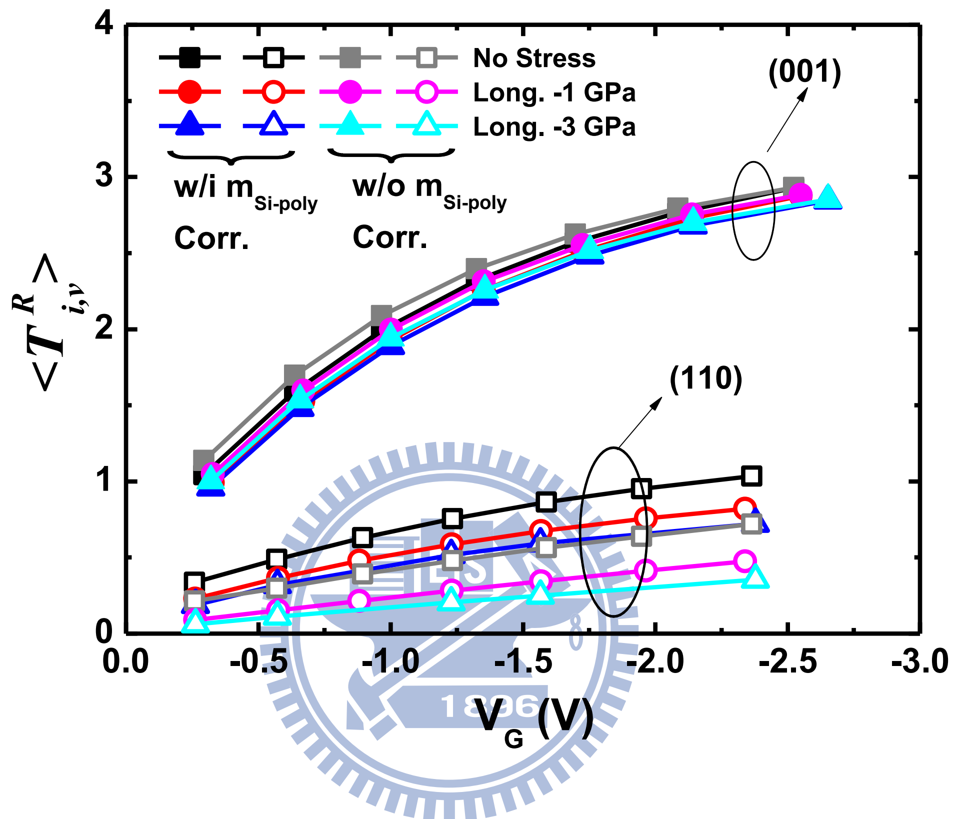

Fig. 3.2.2.5 The contribution of the average reflection part of transmission probability through insulator for (001) and (110) p-MOSFETs under the longitudinal stress conditions of 0, -1, and -3 GPa.

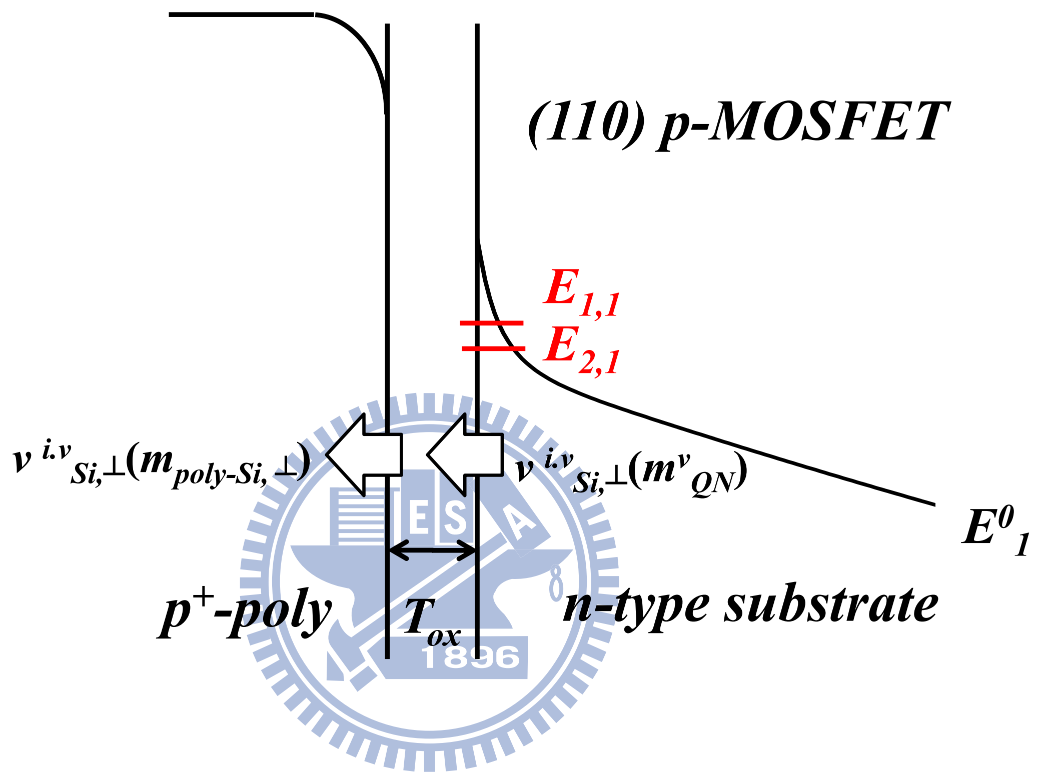

Fig. 3.2.2.6 Schematic of energy band diagram of (110) p-MOSFET to show the effective mass correction in p+-poly gate region. The two group velocities are associated with the effective masses labeled.

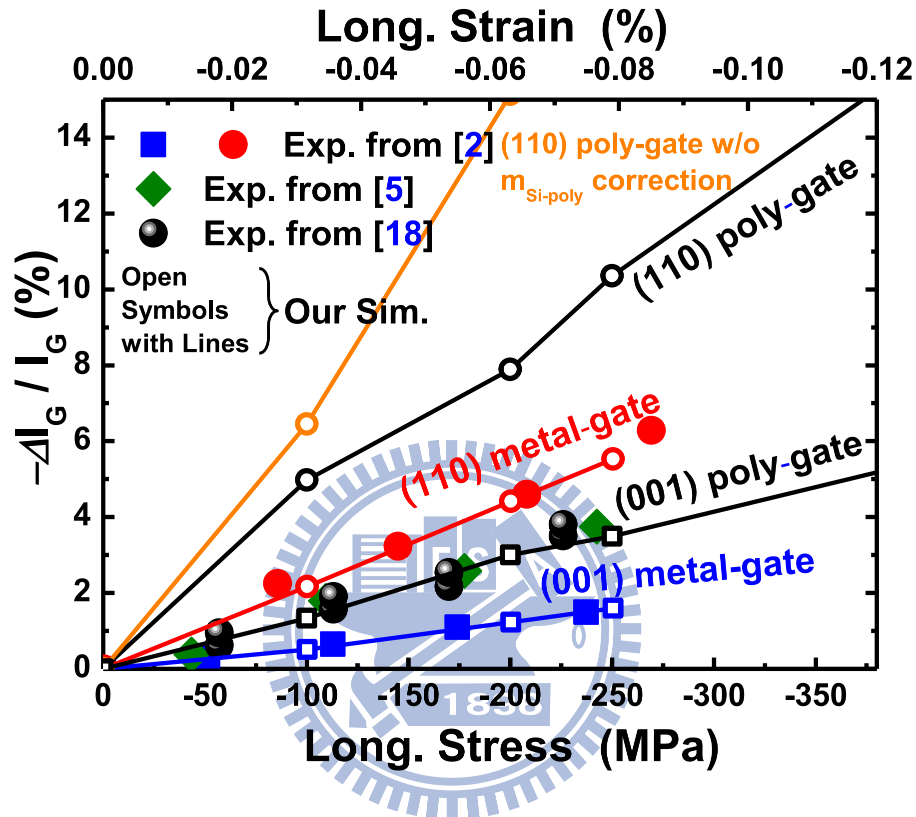

Fig. 3.2.2.7 The comparison of experimental and calculated hole gate direct tunneling current change versus stress. The bias conditions and process parameters in the calculation are close to the experimental ones, where $|V_G|$~1V for polygate and $|V_G|$~1.6V for metal gate.

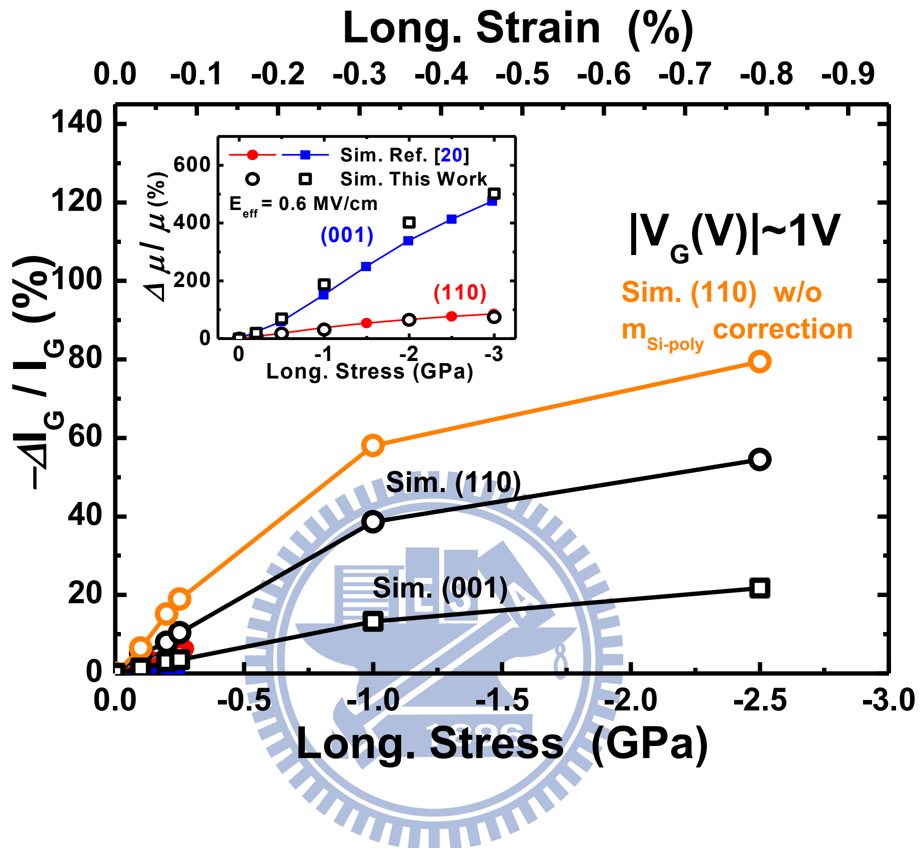

Fig. 3.2.2.8 The calculated hole gate direct tunneling current change as in Fig. 3.3.2.7 but with the stress range largely widened. The inset shows simulated mobility enhancement and its comparison with [20].

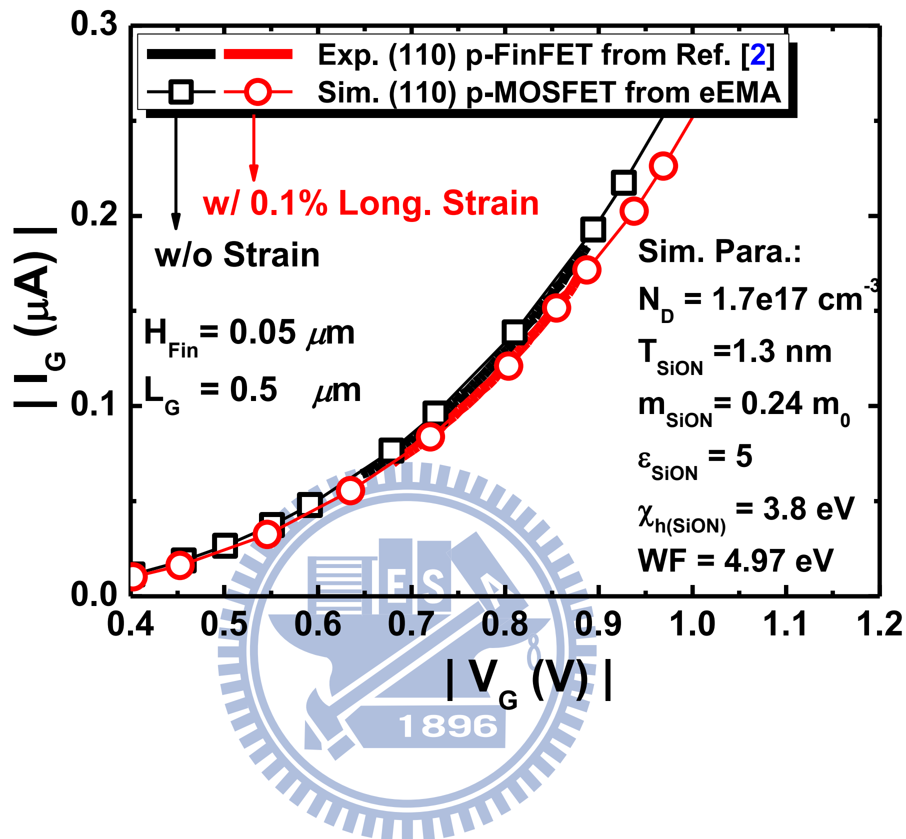

Fig. 3.2.2.9 The comparison of calculated hole gate direct tunneling current for p-FinFET with those measured from (110) sidewall surface p-FinFET [2].

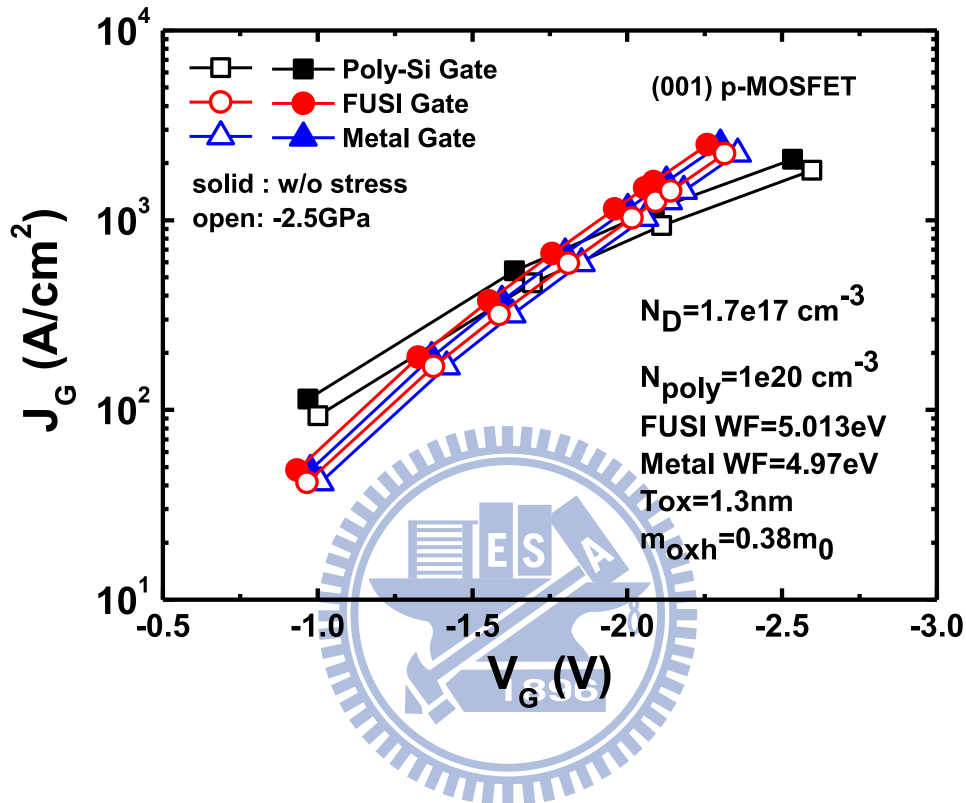

Fig. 3.2.2.10 The calculated hole gate direct tunneling current density for (001) p-MOSFETs with polysilicon, FUSI and metal gates under the longitudinal stress conditions of 0 and -2.5 GPa.

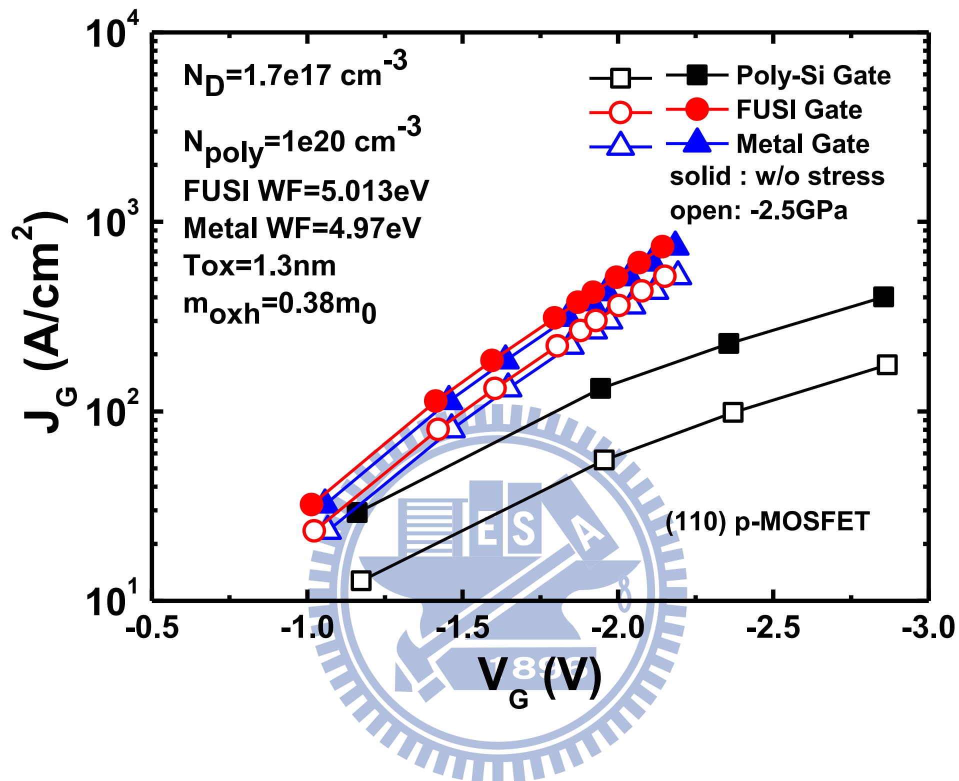

Fig. 3.2.2.11 The calculated hole gate direct tunneling current density for (110) p-MOSFETs with polysilicon, FUSI and metal gates under the longitudinal stress conditions of 0 and -2.5 GPa.

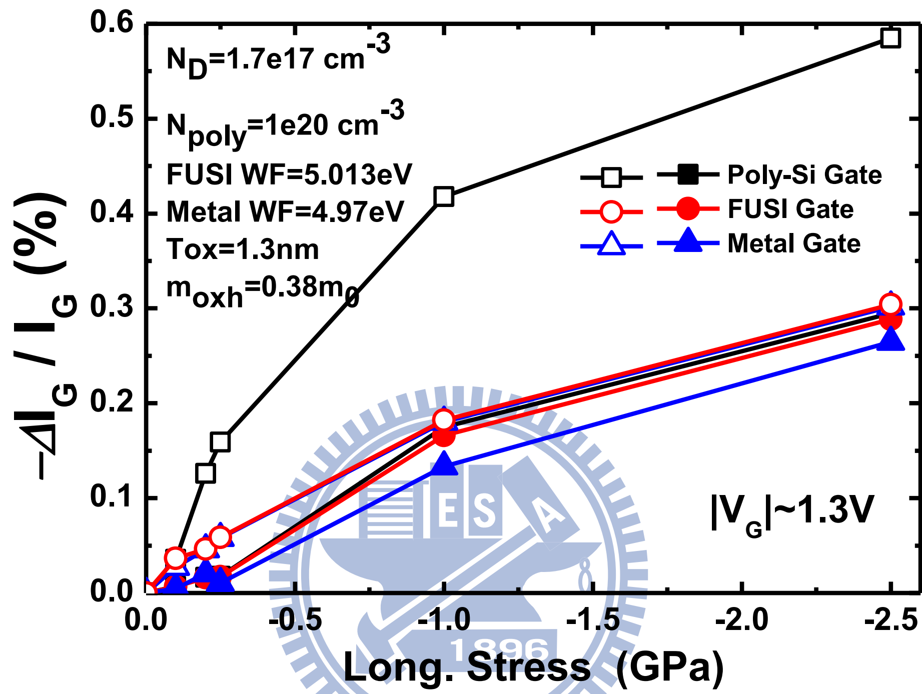

Fig. 3.2.2.12 The calculated hole gate direct tunneling current change versus stress for (001) and (110) p-MOSFETs with polysilicon, FUSI and metal gates.

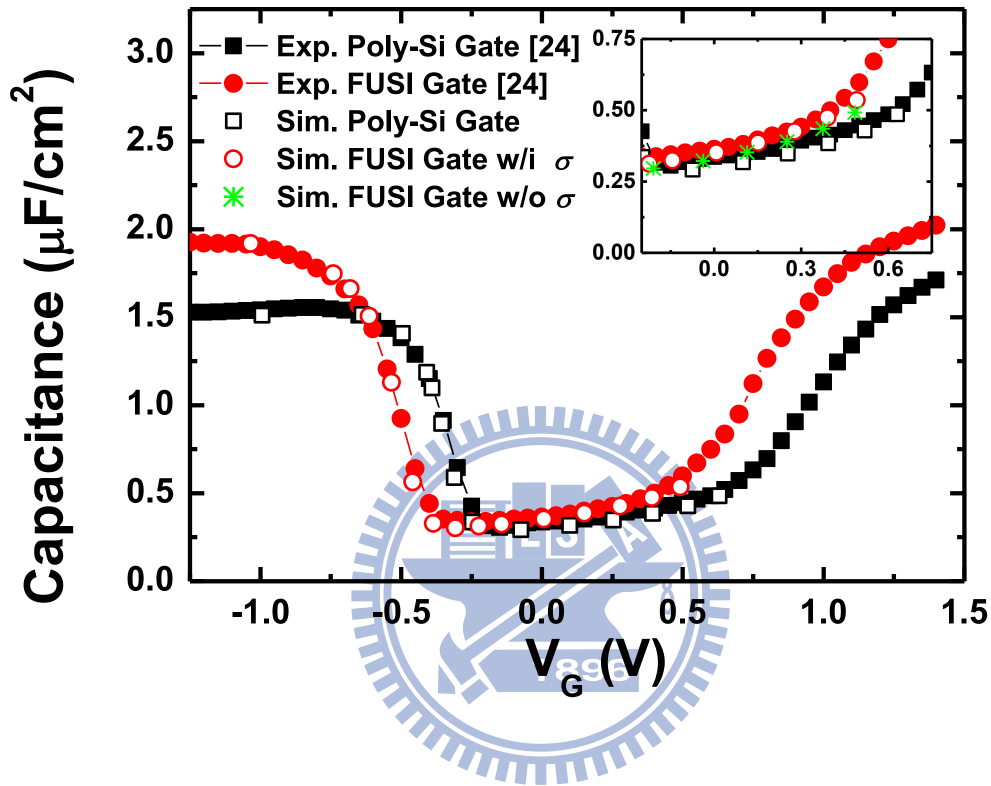

Fig. 4.2.1 Capacitance-voltage fitting through proposed eEMA on (100) p-MOSFETs with polysilicon and FUSI gates. The experimental data is measured under large devices. FUSI imposes an extra compressive stress ~460 MPa on the underlying p-MOSFET channel region. Table I shows the extracted parameters.

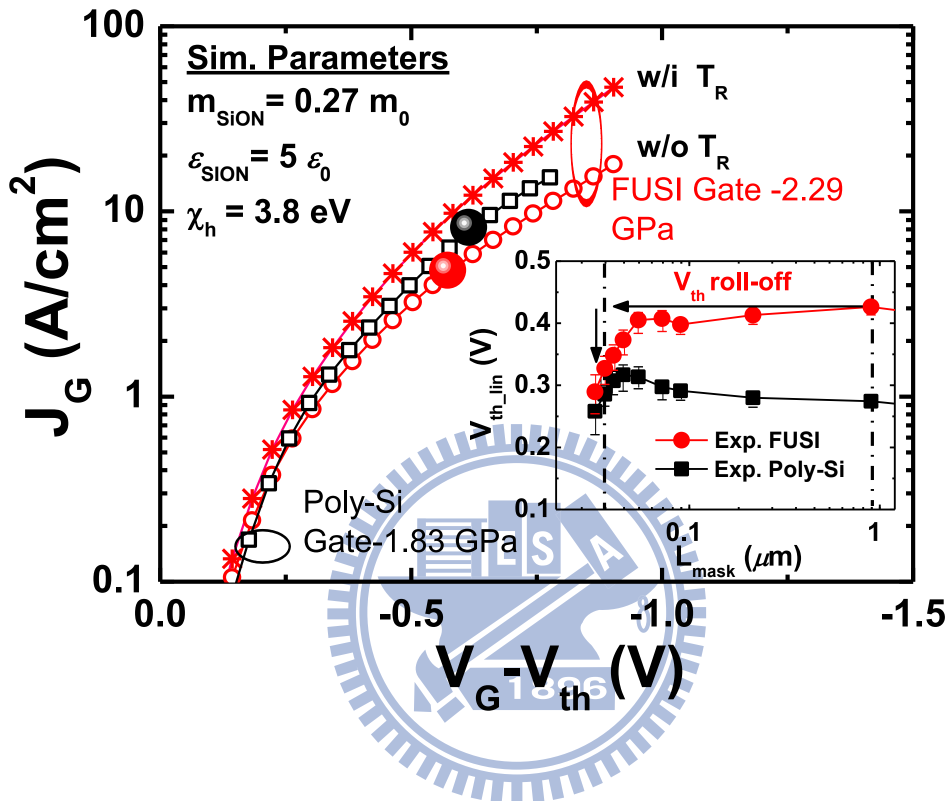

Fig. 4.2.2 Jg versus gate overdrive fitting under the small dimension samples. Solid symbols indicate the experimental data and open symbols with line indicate the calculated one. The gate overdrive is used to eliminate Vth roll-off appearing in FUSI gate as shown in insert, so both the inversion conditions are same: Vth(Lmask=1um) for the ideal calculation results and Vth(Lmask=0.036um) for the experimental results.

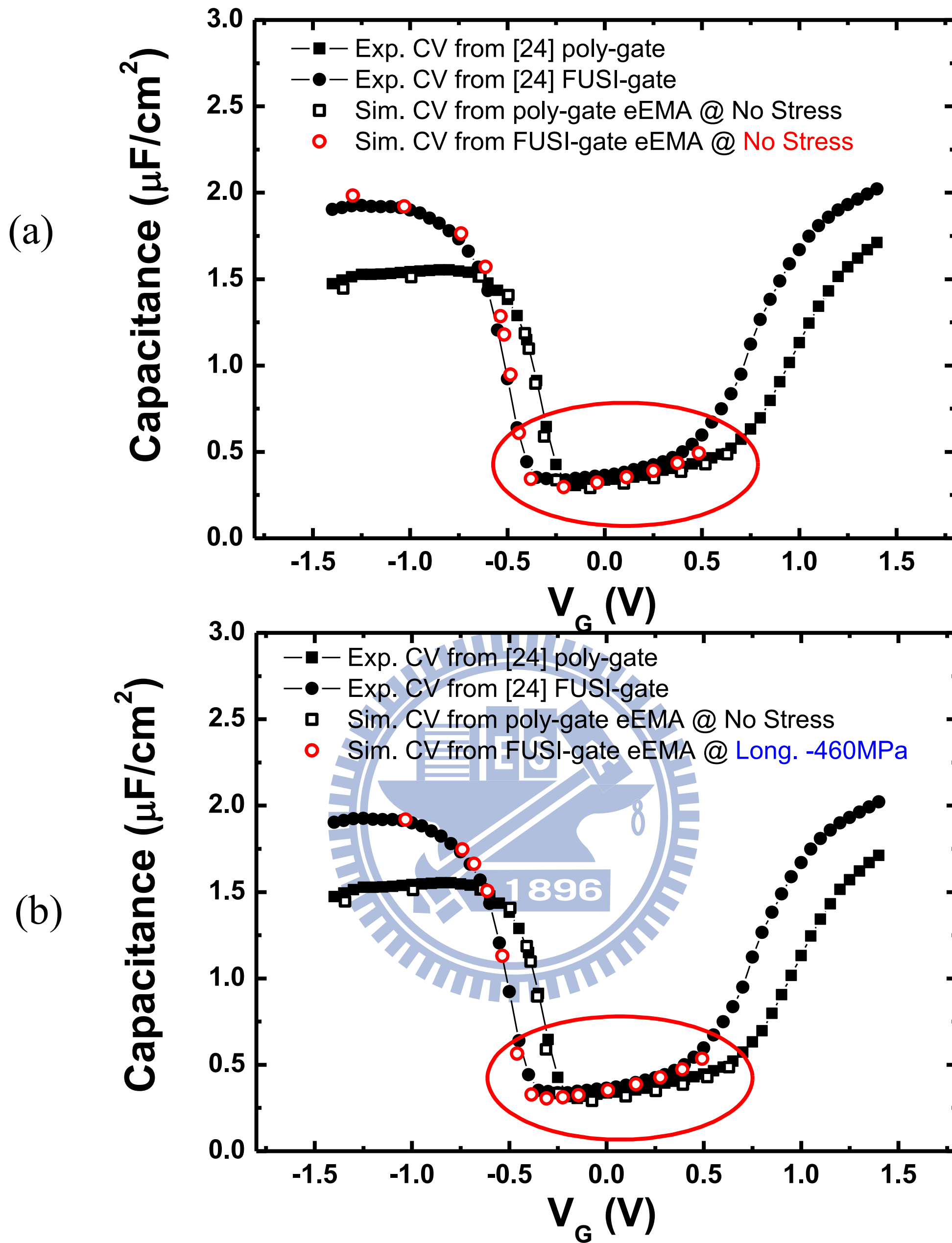

Fig. 4.3.1 Comparison of CV fitting on (100) p-MOSFETs with polysilicon and FUSI gates. (a) without consideration of stress on FUSI gate. (b) Longitudinal compressive stress 460 MPa considered on FUSI gate, which fitted perfectly.

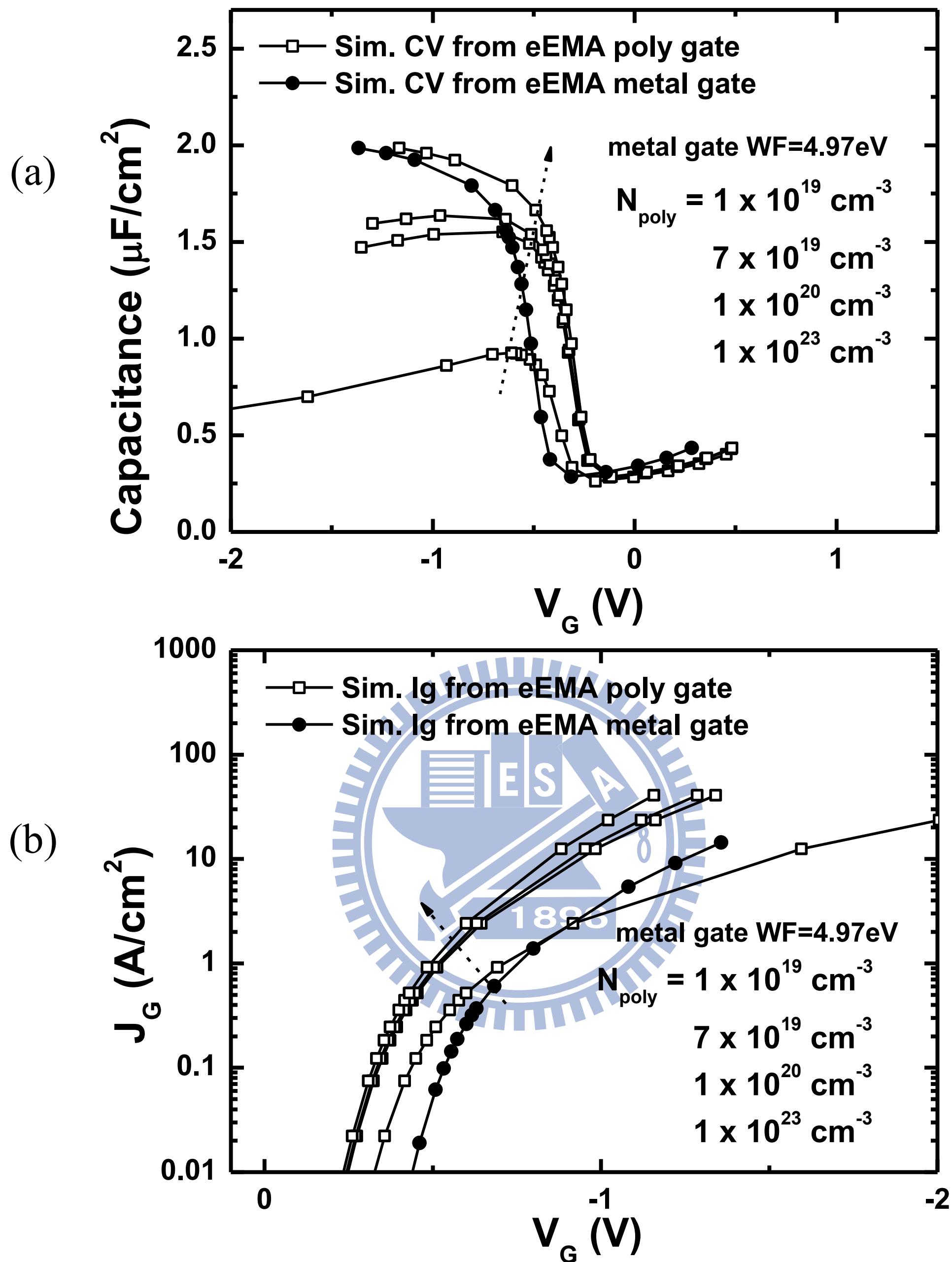

Fig. 4.3.2 Impact of polysilicon dopant concentration on (a) capacitance-voltage curve and (b) Ig versus Vg . $N_{sub} = 1 \times 10^{18} cm^{-3}, T_{ox} = 1.3nm, m_{oxh} = 0.37m_0$, Stress = Long. −1.83 GPa.

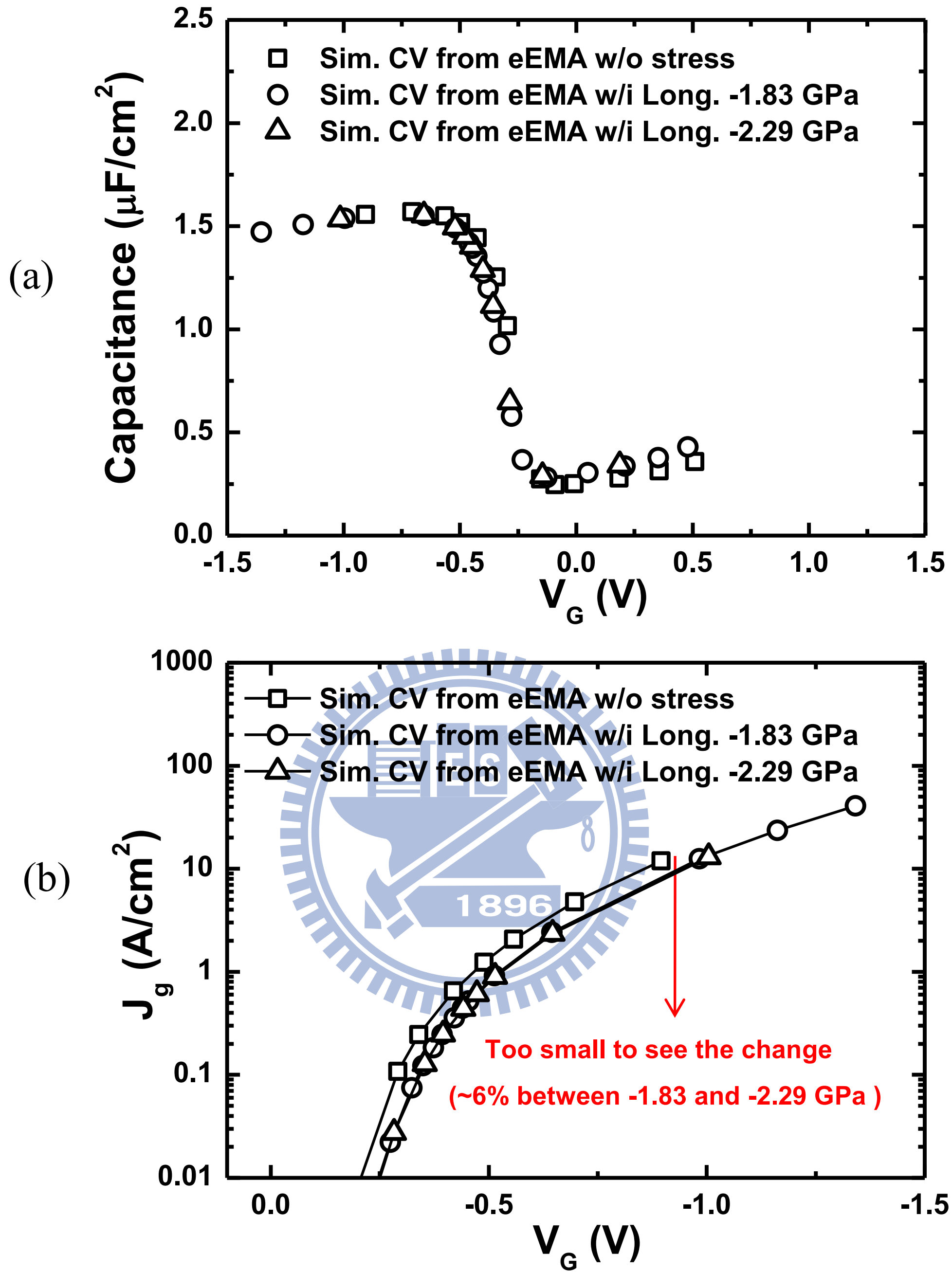

Fig. 4.3.3 Impact of Longitudinal compressive stress on (a) capacitance-voltage curve and (b) Ig versus Vg . $N_{sub} = 1 \times 10^{18} cm^{-3}, T_{ox} = 1.3nm\,, m_{oxh} = 0.37m_0\,, N_{poly} = 7 \times 10^{19} cm^{-3}$.

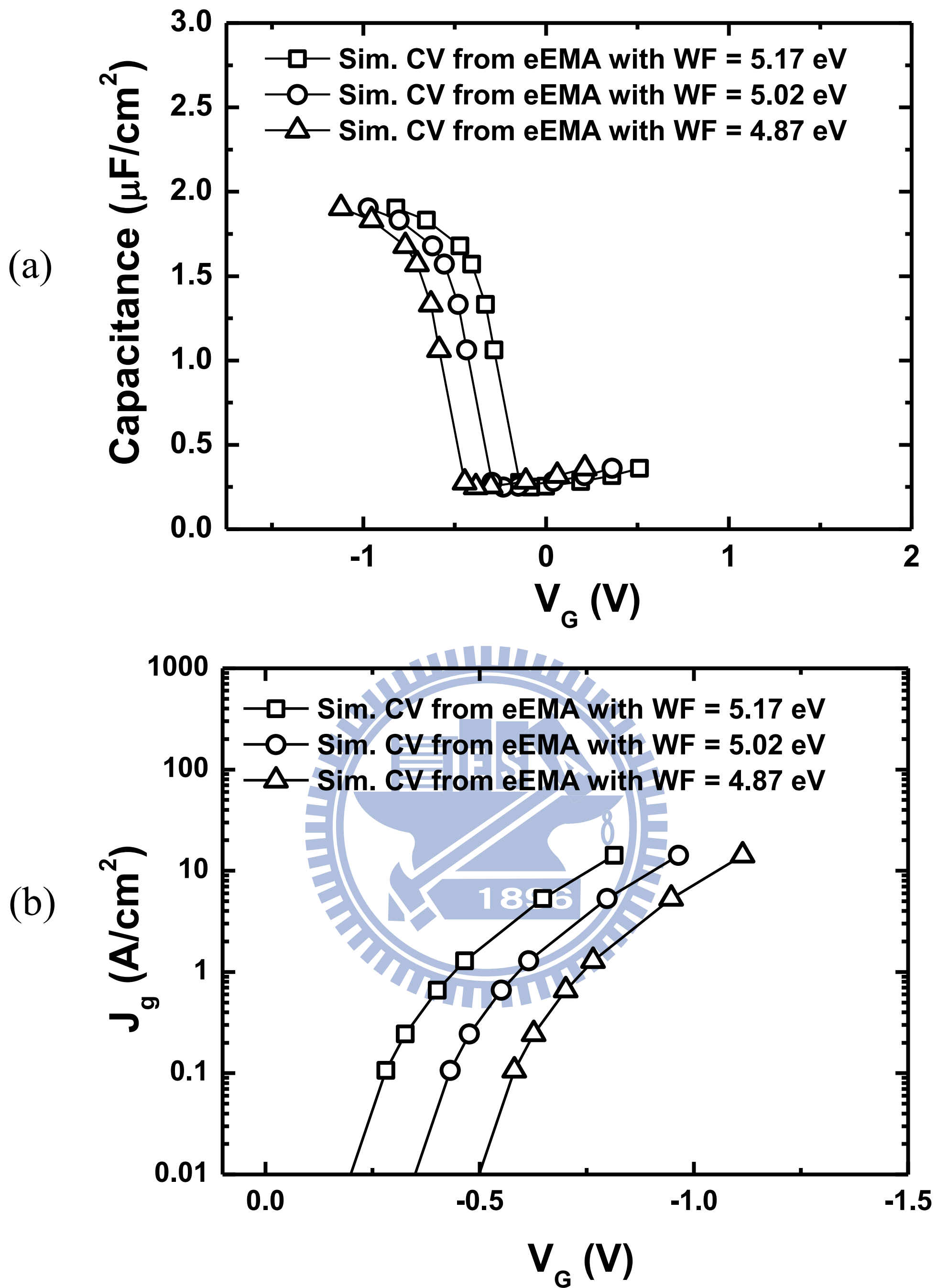

Fig. 4.3.4 Impact of work function shift on (a) Capacitance-voltage curve and (b) Ig versus Vg . $N_{sub} = 1 \times 10^{18} cm^{-3}, T_{ox} = 1.3nm, m_{oxh} = 0.37m_0$, without stress.

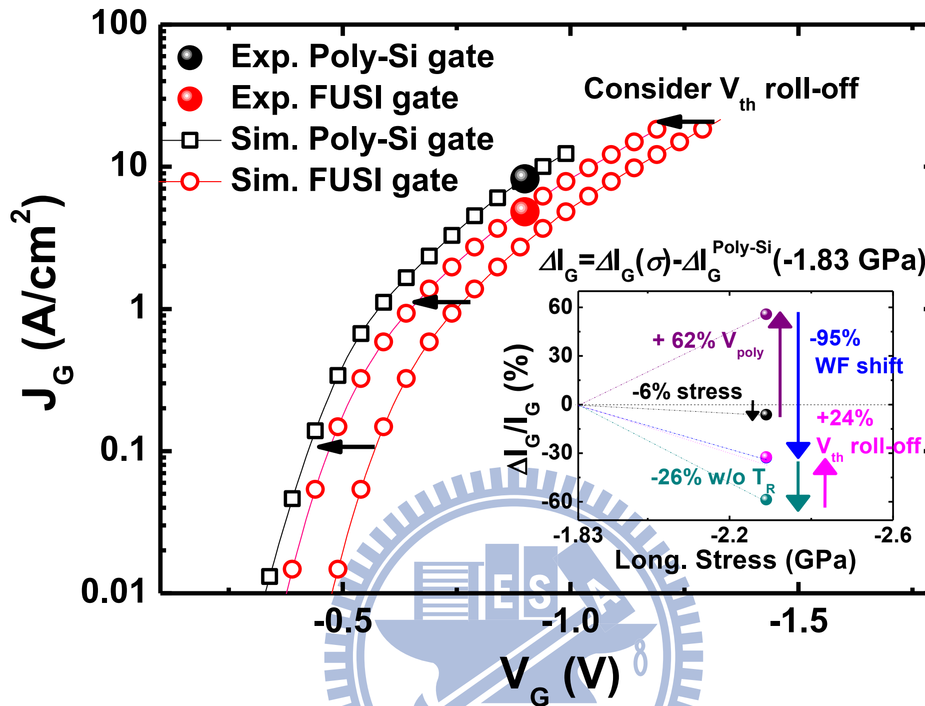

Fig. 4.3.5 The calculated hole gate direct tunneling currents for polysilicon- and FUSI-gate p-MOSFETs and the comparison with two data points [24]. The inset depicts the five main contributions for the observed hole gate direct tunneling current difference.

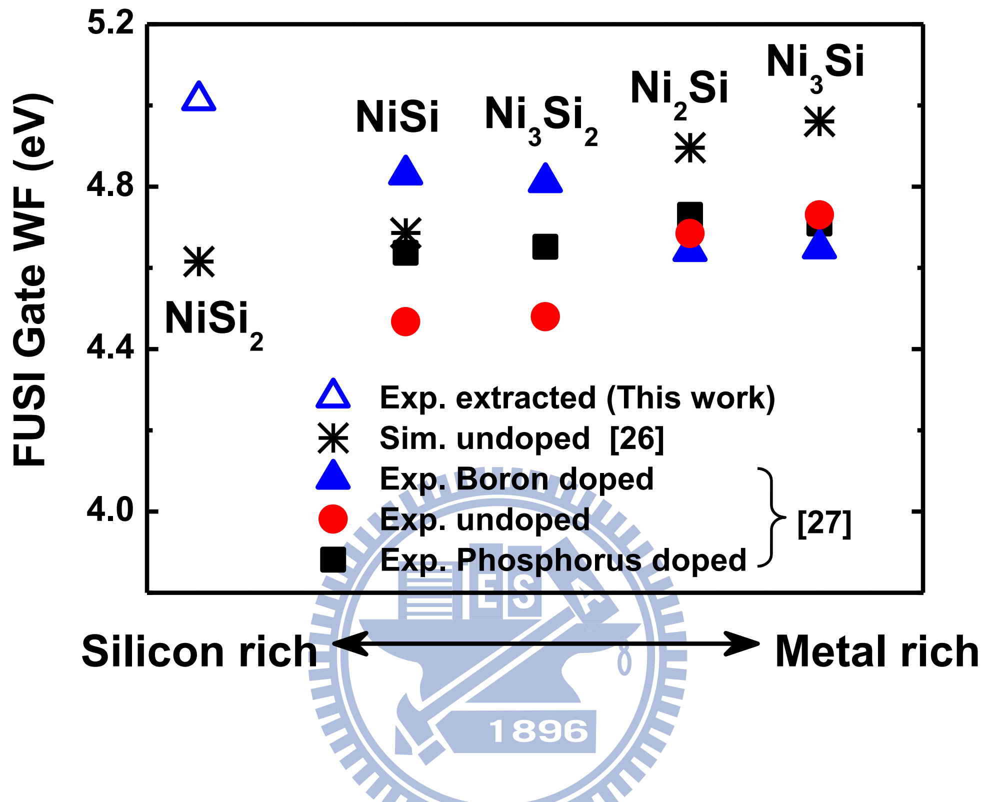

Fig. 4.3.6 The comparison of work function of Ni FUSI gates among this work, [26] and [27]. The additional dopants to polysilicon before silicidation result the shifts in work function.